FET fusion oncoproteins disrupt physiologic DNA repair networks in cancer

Shruti Menon[1,2]*, Daniel Gracilla[1,2]*, Marcus R. Breese[3], Yone Phar Lin[3], Filemon Dela Cruz[2], Tamar Feinberg[2], Elisa de Stanchina[2], Ana-Florina Galic[2], Hannah Allegakoen[3], Shruthi Perati[3], Nicholas Wen[1], Ann Heslin[3], Max A. Horlbeck[4], Jonathan Weissman[5], E. Alejandro Sweet-Cordero[3], Trever G. Bivona[6, 7], Asmin Tulpule[1,2 #]

Affiliations:
[1] Tow Center for Developmental Oncology and Human Oncology and Pathogenesis Program, Memorial Sloan Kettering Cancer Center, 1275 York Avenue, New York, NY, 10021.
[2] Department of Pediatrics, Memorial Sloan Kettering Cancer Center, 444 East 68th Street, 9th Floor, New York, NY 10065.
[3] Division of Pediatric Oncology, University of California, San Francisco, San Francisco, CA 94143.
[4] Division of Genetics and Genomics, Boston Children's Hospital, Boston, MA, 02115.
[5] Department of Biology, Massachusetts Institute of Technology, 77 Massachusetts Ave, 68-132, Cambridge, MA 02139.
[6] Division of Hematology and Oncology, University of California, San Francisco, San Francisco, CA 94143.
[7]Chan Zuckerberg Biohub, San Francisco, CA 94158.
*Denotes equal contribution.
[#]Correspondence to: Asmin Tulpule MD PhD, tulpulea@mskcc.org

Abstract

While oncogenes promote cancer cell growth, unrestrained proliferation represents a significant stressor to cellular homeostasis networks such as the DNA damage response (DDR). To enable oncogene tolerance, many cancers disable tumor suppressive DDR signaling through genetic loss of DDR pathways and downstream effectors (e.g., ATM or p53 tumor suppressor mutations). Whether and how oncogenes can help "self-tolerize" by creating analogous functional defects in physiologic DDR networks is not known. Here we focus on Ewing sarcoma, a FET fusion oncoprotein (EWSR1-FLI1) driven pediatric bone tumor, as a model for the class of FET rearranged cancers. Native FET family members are among the earliest factors recruited to DNA double-strand breaks (DSBs), though the function of both native FET proteins and FET fusion oncoproteins in DNA repair remains to be defined. We discover that the EWSR1-FLI1 fusion oncoprotein is recruited to DNA DSBs and interferes with native FET (EWSR1) protein function in activating the DNA damage sensor ATM. In multiple FET rearranged cancers, FET fusion oncoproteins induce functional ATM defects, rendering the compensatory ATR signaling axis as a collateral dependency and therapeutic target. More generally, we find that aberrant recruitment of a fusion oncoprotein to sites of DNA damage can disrupt physiologic DSB repair, revealing a mechanism for how growth-promoting oncogenes can also create functional defects within tumor suppressive DDR networks.

Main

The DNA damage response (DDR) is a tightly regulated and redundant network that tailors specific repair complexes to address a diverse set of genotoxic insults[1]. In cancer, oncogene-induced hyper-proliferation and replication stress activate the DDR which can trigger senescence or cell death programs[2,3]. Thus, the physiologic DDR represents an important barrier to oncogenic transformation and genetic loss of tumor-suppressive DDR pathways or downstream effectors are frequent cooperating events in cancer (e.g., ATM or p53 mutations)[4,5]. Loss of these DDR genes can also create collateral dependencies and therapeutic opportunities in specific cancers as exemplified by the use of poly-ADP ribose polymerase (PARP) inhibitors to target defective homologous recombination (HR) repair in BRCA1/2 mutant breast and ovarian cancers[6,7]. Outside of HR deficient cancers, while multiple synthetic lethal DDR dependencies have been described (e.g., oncogene-induced replication stress and ATR[3]), the clinical benefit of DDR-targeting therapies is less established and the mechanisms underlying many of these aberrant DDR dependencies remain to be defined[8]. More generally, whether and how oncogenes themselves impair physiologic DNA repair to create functional deficiencies within tumor suppressive DDR networks is poorly understood.

The FET family of intrinsically disordered proteins (FUS, EWSR1, TAF15) are frequent 5' oncogenic transcription factor (TF) fusion partners in a diversity of sarcomas and leukemias[9]. These TF fusion oncoproteins are often the sole oncogenic driver alteration in these cancers and due to the difficulty in pharmacologic targeting of TFs, precision medicine approaches have been lacking. The most studied cancer in this class is Ewing sarcoma (ES), a pediatric bone tumor driven by the EWSR1-FLI1 TF fusion oncoprotein. Patients with relapsed or metastatic ES continue to have dismal outcomes despite maximally intense combination cytotoxic chemotherapy regimens[10]. Paradoxically, decades of clinical experience and laboratory testing of ES cancer cell lines have shown ES to be among the most chemo- and radiosensitive cancers[11-

[14], at least initially. It has long been hypothesized that ES tumors harbor an intrinsic DNA repair defect that explains their underlying sensitivity to DNA damaging therapies. The prevailing model is that ES belongs to a family of "BRCA-like" tumors that are functionally deficient in BRCA1 (due to sequestration of BRCA1 protein by RNA-DNA hybrid structures known as R-loops) and therefore defective in HR double-strand break (DSB) repair[15]. However, both xenograft studies[13] and clinical trials in ES patients[16] failed to demonstrate any benefit for PARP inhibitor monotherapy, in stark contrast to the impressive clinical responses seen across HR deficient BRCA mutant and BRCA-like cancers[17,18]. Thus, the precise nature of the DNA repair defect in ES remains uncertain.

Native FET family proteins contain an N-terminal intrinsically disordered region (IDR) required for interactions amongst FET family members and a C-terminal domain with positively charged RGG (arginine-glycine-glycine) repeats, which mediate recruitment to DSBs via high affinity interactions with negatively charged poly-ADP ribose (PAR) molecules[19,20]. All 3 FET members are rapidly recruited to DSBs in a PARP-dependent manner[20,21], where they undergo liquid-liquid phase separation that is thought to enable compartmentalization of DSB repair proteins[22-24], though the specific role of FET proteins in DSB repair is not well defined. Interestingly, all oncogenic FET fusion proteins including EWSR1-FLI1 share a similar structure: the N-terminal IDR of the FET protein fused to the DNA binding domain of a transcription factor (e.g., FLI1), with loss of the C-terminal RGG repeats[25].

In this study, we address the role of the oncogenic fusion protein EWSR1-FLI1 in regulating the DNA damage response in ES. Contrary to the current classification of ES as a BRCA-like tumor with defective HR[15], we identify functional ATM defects as a principal DDR lesion in ES cells and define the mechanistic basis for FET fusion oncoprotein mediated DNA repair defects across this class of cancers. More broadly, our findings demonstrate how an oncogene that drives cellular transformation can also interfere with physiologic DNA damage repair.

Results

ES cells are dependent on HR factors for survival.

To address the uncertainty surrounding putative DNA repair defect(s) in ES, we set out to identify genes that modulate ES cell survival in response to doxorubicin, a DNA DSB-inducing agent and major component of current chemotherapy regimens[26] (Fig. 1A). We selected a CRISPR interference (CRISPRi) based screening approach given the concern of studying DSB repair phenotypes using an active Cas9 that generates DSBs[27]. Surprisingly, we found that key HR factors BRCA1 and PALB2 were essential for the growth of ES cells even in the absence of doxorubicin (Fig. 1B). Given the prevailing model that ES tumors are functionally HR-deficient, BRCA-like tumors[15], the screen results were unexpected. We validated the finding of HR factor dependency in ES using two independent guide RNAs (gRNAs) against BRCA1 and PALB2 in the screening cell line (A673) and two additional ES cell lines TC-252 and ES-8 (Figs. 1C-E and S1A, B). The same BRCA1 and PALB2 gRNAs had limited effects on cell growth in two non-ES cancer cell lines, which was consistent with the set of published CRISPRi screens[27-29] and suggests the observed dependency on HR factors may be specific to ES cells (Figs. S1C, D). To test the role of EWSR1-FLI1 in inducing this dependency, we utilized an ES cell line with a doxycycline-inducible shRNA against EWSR1-FLI1[30] (Fig. S1E). EWSR1-FLI1 knockdown rescued the growth defects caused by BRCA1 or PALB2 loss, confirming that the oncogenic fusion protein is necessary for the observed dependency on HR factors in ES cells (Fig. 1F).

CRISPRi screening also identified genes whose loss sensitized ES cells to doxorubicin including LIG4, NHEJ1 (XLF), and 53BP1 (Fig. S1F). The presence of key canonical non-homologous end joining (c-NHEJ) genes as top chemo-sensitizer hits validated our experimental approach as this pathway is critical for repairing both drug and ionizing radiation (IR)-induced DSBs and provides evidence for a functional c-NHEJ pathway in ES cells. The list of top chemosensitizer genes included Aurora Kinase A (AURKA), for which inhibitors are under clinical development[31], and the

E3 Ubiquitin Ligase RNF8, both of which could be targeted in combinatorial therapeutic approaches with doxorubicin-based treatment regimens. The final category of screen hits were genes whose loss promoted survival under high doses of doxorubicin (LD97), mirroring the residual disease state in ES patients (Fig. S1G). SLFN11 is a notable hit as loss of SLFN11 has been shown to promote chemotherapy resistance in multiple cancer subtypes including ES[32,33]. The complete screen results are provided in Supplementary Table 1 (see Supplemental Note 1 for discussion of DepMap results). Given the paradoxical finding of HR factor dependence in ES, we chose to focus on the regulation of DSB repair in ES and whether ES tumors are properly classified as BRCA-like cancers.

ES patient tumors do not display the genomic scars of HR deficiency.

We next directly examined genomic DNA from 100 ES patient tumor samples[34] for evidence of functional HR deficiency. This is a validated strategy in BRCA1/2 mutant and BRCA-like tumors wherein defective HR repair results in specific genomic scars that result from increased utilization of compensatory pathways such as alternative end-joining (alt-EJ) and single-strand annealing (SSA)[35,36]. We developed a custom bioinformatics pipeline to analyze the genomic landscape of ES tumor genomes, using BRCA1/2 mutant and wild-type breast cancer genomes (from EGAD00001001322[35]) to validate our algorithms. The ES cohort was reported in Tirode et al to represent diagnostic, pre-treatment biopsies of the primary tumor site, with 63% of patients having localized disease[34]. The ES whole genome sequencing data were previously deposited in the European Genome-phenome Archive (EGAS00001000855, EGAS00001000839).

At least thirty mutational signatures have been identified in human cancers with Signature 3 being the most highly associated with BRCA1/2 mutant cancers[35]. Our analysis confirmed high levels of Signature 3 in BRCA mutant as compared to BRCA wild-type tumors but did not show increased levels of Signature 3 in ES tumors (Figs. 2A and S2A). In addition to increased Signature 3,

BRCA1/2 mutant tumors displayed an increase in the number and size of deletions compared to BRCA wild-type tumors (Figs. 2B, C and S2B-D) consistent with previous reports[35]. ES tumors are clearly distinct from BRCA1/2 mutant tumors displaying few deletions per genome and a size distribution skewed further towards small deletions than even BRCA wild-type tumor samples (Figs. 2B, C and S2B-D).

We further examined the sequences flanking deletion sites for short stretches of overlapping microhomology (MH). Defective HR repair in BRCA mutant or BRCA-like tumors results in increased usage of the error prone DSB repair pathway alt-EJ that employs MH for initial annealing of resected DSB ends[37]. We utilized BRCA mutant/wild-type samples to computationally define deletion size bins and identified an increase in the proportion of intermediate size deletions (7-28 base pairs (bp), 29-45 bp) in BRCA mutant samples as reported previously (Figs. S2E, F). We then verified a significant increase in breakpoint MH at intermediate size (7-28bp and 29-45bp) deletions in BRCA mutant tumors compared to wild-type and no increase in MH at small deletions (1-6bp) where c-NHEJ predominates (Figs. 2D, E, and S2E-G), both consistent with published findings[35]. ES samples clustered with BRCA wild-type tumors and display a trend toward even less MH-mediated DSB repair than BRCA wild-type samples (Figs. 2D, E, and S2G). Our findings in ES were independent of the recurrent STAG2 and p53 mutations that occur in a subset of these cancers (Figs. S2H, I). Taken together, these results demonstrate that ES patient tumors do not display the genomic signatures of BRCA1/2 mutant cancers and lack the footprint of isolated HR deficiency.

EWSR1-FLI1 impairs resection-dependent DSB repair.

The absence of HR deficient genomic scars in ES tumors and paradoxical requirement of HR factors for ES cell survival prompted us to systematically re-examine how EWSR1-FLI1 impacts DSB repair pathway utilization (Fig. 3A). We posited that previous reports of defective HR in ES

might alternatively be explained by a more general upstream defect in DSB repair. We utilized a set of well-established DSB repair reporter cell lines wherein expression of the I-SceI endonuclease induces a DSB within an interrupted GFP reporter cassette, such that utilization of a particular DSB repair pathway restores a GFP coding sequence enabling a quantitative readout of individual repair pathway efficiency[38]. Nucleofection of EWSR1-FLI1 into each reporter cell line was performed using a BFP-expressing, dual promoter plasmid, followed by expression of mCherry-I-SceI after 24 hours to induce a single DSB (Figs. S3A, B). The use of fluorescently tagged plasmids enabled detection of DSB repair specifically in cells that expressed both EWSR1-FLI1 (or empty vector) and I-SceI (Fig. S3A).

To examine HR repair, we utilized the DR-GFP reporter and observed a reduction in HR upon EWSR1-FLI1 expression, consistent with previous reports[15] (Fig. 3B). However, EWSR1-FLI1 expression also reduced the efficiency of MH-mediated alt-EJ repair (EJ2) and long-stretch MH mediated-SSA repair (Figs. 3C, D and S3C). EWSR1-FLI1 mediated reductions in HR, alt-EJ, and SSA repair efficiency were intermediate compared to knockdown of the key end-resection factor CtIP that is required for all resection-dependent DSB repair[39] (Figs. 3C, D and S3C). These data indicate EWSR1-FLI1 expression does not result in isolated HR defects, but instead compromises all three resection-dependent DSB repair pathways.

We also evaluated c-NHEJ, a fast-acting DSB repair pathway which does not require end-resection, using the EJ5 reporter system. We observed an increase in the usage of c-NHEJ upon EWSR1-FLI1 expression (Fig. 3E) consistent with our CRISPRi screen findings of an intact c-NHEJ pathway (Fig. S1F) and the increased frequency of small deletions observed in ES patient samples (Fig. 2C). Using a distinct I-SceI based DSB repair reporter[40], we directly examined the junctional sequences after DSB induction for evidence of cNHEJ or MH-mediated alt-EJ repair (HR and SSA events are not evaluable in this system) and confirmed an increase in cNHEJ and decrease in alt-EJ upon expression of EWSR1-FLI1 (Fig. S3D). We verified that the repair

phenotypes were not the result of EWSR1-FLI altering cell cycle profiles or causing a cell cycle arrest in these short-term assays (Figs. S3E, F).

To assess how EWSR1-FLI1 regulates the transcription of DDR genes that control resection-dependent DSB repair, we analyzed published RNA-sequencing data in ES cells before and after EWSR1-FLI1 knockdown[41] (Fig. S3G). Interestingly, we found that EWSR1-FLI1 either increased or had minimal effect on the expression of key genes involved in resection-dependent DSB repair (MRE11, CtIP, BRCA1/2, PALB2, RAD52, POLQ), and had no effect on expression of many c-NHEJ genes (LIG4, NHEJ1). We also analyzed published quantitative proteomics data from the Cancer Cell Line Encyclopedia[42] and found nearly all major DNA repair proteins were expressed across 4 ES cell lines and no evidence for a state of low/absent DNA repair factors that would explain the observed effects on resection-dependent repair (Supplementary Table 2). These data suggest that EWSR1-FLI's effect on DSB repair pathway utilization is not the result of transcriptional downregulation of key end-resection and resection-dependent DSB repair genes (e.g., BRCA1) by the fusion oncoprotein. In summary, we demonstrate that EWSR1-FLI1 does not induce isolated HR deficiency but instead compromises all three resection-dependent DSB repair pathways.

ATM activation and signaling is impaired by the Ewing sarcoma fusion oncoprotein

To explain our finding that EWSR1-FLI1 impairs multiple branches of resection-dependent DSB repair, we focused on the upstream regulation of the DDR and end-resection in ES cells (Fig. 3A). The DDR is a partially redundant signaling network regulated by three kinases, DNA-PK, ATM, and ATR, each of which control distinct aspects of DDR signal amplification and DSB pathway choice. ATM was a logical candidate since it promotes DNA end-resection and HR[43], and ATM loss creates a synthetic lethal dependence on HR proteins[44,45]. We therefore tested whether EWSR1-FLI1 affects the activation and function of these three apical DDR kinases.

We utilized 3 distinct ES cell line models with inducible EWSR1-FLI1 depletion: A673 and TC-32 ES cells with doxycycline-inducible shRNA's targeting EWSR1-FLI1 (either the junctional sequence or the 3' FLI1 portion of the fusion, see Methods)[30] and A673 "EWSR1-FLI1 degron" cells with an auxin-inducible degron (AID) tag inserted at the endogenous EWSR1-FLI1 locus enabling rapid depletion of the fusion oncoprotein[46]. Consistent across all three ES cell models, depletion of EWSR1-FLI1 increased both ATM activation (autophosphorylation) and downstream ATM signaling (phosphorylation of key downstream targets CHK2 and KAP1) in response to ionizing radiation (IR) (Figs. 4A-D and S4A, B). In contrast, activation of the other apical DDR kinases (DNA-PK, ATR) was not affected by EWSR1-FLI1 knockdown in ES cells (Figs. S4C-S4F). There were differences between the three model systems; KAP1 phosphorylation increased significantly only at later time points (3 and 6 hours) in A673 shEWSR1-FLI1 cells, whereas the p-KAP1 effects were also present at the 1-hour timepoint in A673 "EWSR1-FLI1 degron" cells which have greater levels of EWSR1-FLI1 depletion (Figs. 4A, B, and Figs. S4A, B). Importantly, all three modifications (p-ATM/p-CHK2/p-KAP1) were induced upon irradiation of ES cell lines, indicating EWSR1-FLI1 does not completely suppress ATM functionality.

In the reciprocal experiment, we expressed EWSR1-FLI1 in 2 non-ES cell lines (U2OS cancer cells and mouse embryonic fibroblasts, MEFs) to test whether ectopic EWSR1-FLI1 expression would impair ATM function. In both cell lines, EWSR1-FLI1 suppressed ATM activation (p-ATM) and downstream ATM signaling (p-KAP1/p-CHK2) in response to IR (Figs. 4E-H, see Methods on measuring CHK2 phosphorylation by mobility shift in MEFs[47,48]). Consistent with our findings in ES cells, ectopic EWSR1-FLI1 expression did not impact DNA-PK or ATR activation and signaling (Figs. S4G, H). Absolute p-ATM foci number after IR was not affected by EWSR1-FLI1 (Fig. S4I) and we observed a reduction in gH2AX (gamma-H2AX, the phosphorylated version of Histone H2AX) signal intensity by flow cytometry, but not absolute gH2AX foci number, after IR in EWSR1-FLI1 expressing cells (Figs. 4I and S4J). These data further support an ATM signaling

defect in ES as ATM is the principal DDR kinase responsible for the phosphorylation and amplifying spread of gH2AX surrounding DSBs[43].

Both ATM and ATR coordinate aspects of resection-dependent DSB repair (Fig. 3A) and ATM mutant tumors display synthetic lethality with ATR inhibitors, reflecting the vital compensatory role of the ATR signaling axis in the absence of ATM[49,50]. Given that suppression of ATM by EWSR1-FLI1 is incomplete (i.e., ATM can be activated/signal to some extent in ES cells), we tested whether the functional ATM defects in ES were sufficient to induce a collateral dependence on the ATR signaling axis. Indeed, A673 and TC-32 ES cells displayed nanomolar range sensitivity to the ATR inhibitor elimusertib (IC50's of 28 and 34nM respectively, comparable to cancer cell lines with known pathogenic ATM mutations[51]), and ATR inhibitor sensitivity was significantly reversed by EWSR1-FLI1 knockdown in both cell lines (Figs. 4J, K). EWSR1-FLI1 knockdown also reversed ES cell sensitivity to an inhibitor of ATR's key downstream target, CHK1, and to treatment with the DSB-inducing chemotherapeutic agent doxorubicin (Figs. S4K-M). Lastly, overexpression of RNAseH1 which degrades R-loops, the major source of oncogene-induced replication stress in ES[15], did not alter the ATR inhibitor sensitivity of ES cells (Figs. S4N, O) further indicating that the molecular basis of ATR inhibitor response in ES cells may be a consequence of ATM defects. The collective findings establish an EWSR1-FLI1-dependent specific impairment of ATM function in ES and resultant synthetic lethality with the compensatory ATR signaling axis.

Comparison of EWSR1-FLI1 to canonical ATM activators

To quantify the extent of ATM suppression by EWSR1-FLI1, we benchmarked our effect size to well-characterized activators of ATM including the MRN (MRE11/RAD50/NBS1) complex, MDC1, RNF8 and RNF168[43]. There is a hierarchy amongst genes regulating ATM activity in response to DSBs: the MRN complex is required for ATM activation[52,53] and serves as an upper bound for

effect size, while the scaffolding protein MDC1[54,55] and E3 ubiquitin ligases RNF8[56-58] and RNF168[59,60] have an intermediate phenotype given their important but not essential role in amplifying ATM signaling.

We utilized established MEF models of ataxia telangiectasia-like disease (ATLD)[47] or Nijmegen breakage syndrome (NBS)[61]; human diseases of the MRN complex defined by genomic instability and radiosensitivity and caused by biallelic loss of function mutations in MRE11 or NBS1 respectively. These models allowed us to compare ATM signaling upon EWSR1-FLI1 expression with genetic loss of the MRN complex. As described previously, $MRE11^{ATLD/ATLD}$ and $NBS1^{\Delta B/\Delta B}$ MEFs display significantly decreased ATM autophosphorylation and minimal downstream ATM signaling (p-KAP1/p-CHK2) after IR compared to wild-type controls (Figs. 5A, B), with $NBS1^{\Delta B/\Delta B}$ MEFs displaying a relatively more severe ATM phenotype than $MRE11^{ATLD/ATLD}$ MEFs. EWSR1-FLI1 expression in wild-type MEFs suppressed ATM activation and downstream KAP1 and CHK2 phosphorylation to levels that are 38-56% of the effect size seen with $MRE11^{ATLD/ATLD}$ or $NBS1^{\Delta B/\Delta B}$ MEFs (Figs. 5A, B, E). We note that unlike $MRE11^{ATLD/ATLD}$ or $NBS1^{\Delta B/\Delta B}$ MEFs, the kinetics of ATM activation and CHK2 phosphorylation (as measured by mobility shift[47], see Methods) are not delayed in EWSR1-FLI1 expressing MEF cells, consistent with residual ATM activity.

Additionally, we compared EWSR1-FLI1 expression to the milder ATM phenotypes induced by MDC1 or RNF168 shRNA knockdown in MEFs and observed overall similar levels of suppression in terms of ATM activation and signaling (Figs. 5C-E and S5A, B). There were differences between the trends within the two comparisons; EWSR1-FLI1 expressing MEFs displayed greater suppression of all three markers (p-ATM/p-KAP1/p-CHK2) when compared to RNF168 knockdown, whereas only p-KAP1 was decreased to a greater extent than MDC1 knockdown (though all three markers were still reduced relative to control MEFs). These data reinforce EWSR1-FLI1's significant suppressive effect on ATM activation and signaling with an effect size

comparable to knockdown of MDC1 or RNF168, but not equivalent (38-56%) to the near complete functional ATM deficiency seen with loss of the MRN complex in ATLD or NBS.

To assess the extent of ATM suppression at endogenous EWSR1-FLI1 levels in ES cells, we utilized the A673 "EWSR1-FLI1 degron" system. We compared auxin-induced degradation (AID) of endogenous EWSR1-FLI1 with shRNA knockdown of MRE11, NBS1, MDC1, RNF8, and RNF168. Consistent with the results in MEFs, the presence of EWSR1-FLI1 at endogenous levels suppressed ATM activation and downstream signaling to 29-64% of the levels seen with knockdown of MRN complex genes (Figs. 5F-H, and S5C, D). To make these comparisons, we note that maximal ATM activity after IR was seen in the "shSCR (Scramble)/+Auxin" condition with no MRE11/NBS1 gene knockdown and EWSR1-FLI1 depleted. To benchmark the ATM effects of endogenous EWSR1-FLI1 against MRN complex gene knockdown, we compared reduction from the maximal ATM activity condition (red bars) for (1) "shSCR/no Auxin (blue bars)" where EWSR1-FLI1 is now expressed at endogenous levels (and no MRN gene knockdown) versus (2) "shMRE11 or shNBS1/+Auxin (green bars)" where there is MRN gene knockdown (but EWSR1-FLI1 remains depleted).

In comparisons with MDC1 and the E3 ubiquitin ligases RNF8 and RNF168, endogenous levels of EWSR1-FLI1 suppressed ATM activation and signaling to overall similar levels to loss of MDC1, RNF8, or RNF168 (Figs. 5F, I, J, and S5D-G). There was again variation between the markers with endogenous EWSR1-FLI1 having comparable (or slightly greater) levels of p-ATM and p-KAP1 suppression compared to MDC1, RNF8 or RNF168 knockdown, whereas knockdown of MDC1 (but not RNF8 or RNF168) had a greater effect on CHK2 phosphorylation than endogenous EWSR1-FLI1 consistent with a direct interaction between MDC1 and CHK2[62]. Across all experiments, the combined presence of endogenous EWSR1-FLI1 (no Auxin) and gene knockdown could further suppress ATM activation/signaling even in MRE11 or NBS1 knockdown cells, suggesting non-redundant mechanisms of ATM suppression. Taken together, our results

demonstrate that EWSR1-FLI1 induces functional defects in ATM activation and signaling with an effect size that is not equivalent (~30-60%) to the near complete absence of ATM activity seen with loss of the MRN complex, but comparable to loss of classical ATM activators including MDC1, RNF8, and RNF168 (Figs. 5E, F), thereby contextualizing the effect size and biological significance of the ATM defects in ES.

Loss of native EWSR1 phenocopies the DNA repair defects caused by EWSR1-FLI1.

How does EWSR1-FLI1 regulate DNA repair to create ATM defects? We hypothesized that previously reported interactions between EWSR1-FLI1 and native FET proteins (e.g., EWSR1) may disrupt the putative function of native FET family members in early DSB repair compartmentalization[63,64], thereby impacting ATM activation and downstream signaling. Consistent with prior studies[64], EWSR1-FLI1 and another native FET family member (FUS) coprecipitated with FLAG-tagged EWSR1 (Fig. S6A). The strength of these interactions was unchanged in the setting of the DNA DSB-inducing agent neocarzinostatin (NCS) indicating a high affinity interaction not disrupted by the DDR. Given that native EWSR1 accumulates at laser-induced DSB stripes within seconds[20], we tested whether the aberrant interaction between EWSR1 and EWSR1-FLI1 in ES impacts the kinetics of native EWSR1 recruitment to DNA DSBs.

The initial recruitment of EWSR1 to laser micro-irradiated DSBs was mildly reduced by EWSR1-FLI1 expression in non-ES (U2OS) cells, but with unchanged kinetics. However, EWSR1-FLI1 expression resulted in the premature and rapid clearance of native EWSR1 from DSB stripes (Figs. 6A, B). In the reciprocal experiment using A673 “EWSR1-FLI1 degron” cells, depletion of EWSR1-FLI1 increased the levels of EWSR1 recruitment to laser-induced DSBs across all time points (Fig. S6B). These data suggest EWSR1-FLI1 may interfere or compete with native EWSR1 recruitment and retention at DNA DSB sites.

To determine whether loss of native EWSR1 function at DNA DSBs contributes to EWSR1-FLI1-dependent DNA repair defects, we first characterized the role of native EWSR1 in DSB repair using the pathway-specific DSB repair reporters. Analogous to EWSR1-FLI1 expression, native EWSR1 knockdown decreased all three resection-dependent DSB repair pathways, HR, alt-EJ and SSA (Figs. 6C-E and S6C) without altering cell cycle profiles (Fig. S6D). Interestingly, c-NHEJ efficiency was also reduced upon EWSR1 knockdown (Fig. 6F), highlighting differences between native EWSR1 loss and EWSR1-FLI1 overexpression that may relate to the fast timescale of cNHEJ repair and preserved initial EWSR1 recruitment kinetics despite EWSR1-FLI1 expression (Figs. 6A, B).

We further assessed the role of native EWSR1 in activation of the upstream DDR kinases ATM, DNA-PK, and ATR. Analogous to EWSR1-FLI1 expression, native EWSR1 knockdown reduced activation of ATM itself (autophosphorylation) and downstream ATM signaling (phosphorylation of CHK2 and KAP1) upon IR, again with either no effect (DNA-PK) or mildly increased (ATR) activation of the other two DDR kinases (Figs. 6G, and S6E, F). We also compared knockdown of EWSR1 to depletion of the MRN complex (MRE11 siRNA) to benchmark the ATM effect size and observed similar levels of ATM suppression after IR (Figs. S6G, H; note for these comparisons, the incomplete knockdown of MRE11 resulted in less p-ATM suppression relative to p-KAP1/p-CHK2). Thus, knockdown of native EWSR1 results in significant defects in ATM activation and signaling, but importantly does not completely suppress ATM functionality as all three modifications (p-ATM/p-CHK2/p-KAP1) are still induced upon IR treatment.

We utilized a proximity ligation assay (PLA) to establish an IR-dependent interaction between gH2AX and EWSR1 (Figs. 6H and S6I), further supporting a role for native EWSR1 in coordinating early DSB repair responses. Finally, knockdown of native EWSR1 decreased IR-induced gH2AX signal intensity by flow cytometry, but not gH2AX foci number, analogous to EWSR1-FLI1 overexpression (Fig. 6I). These data define the function of native FET family member EWSR1 as

a specific regulator of ATM activation and signaling. In total, we demonstrate that EWSR1-FLI1 causes premature loss of native EWSR1 from DSBs and DNA repair defects that are largely, but not entirely (see Discussion on cNHEJ), phenocopied by native EWSR1 knockdown.

EWSR1-FLI1 and other FET fusion oncoproteins are recruited to DNA double-strand breaks.

To determine a molecular basis for the ATM defects seen in ES, we asked whether the interaction between native EWSR1 and EWSR1-FLI1 (Fig. S6A) might promote aberrant localization of the fusion oncoprotein to DNA DSBs. Indeed, we discovered that EWSR1-FLI1, like native EWSR1, is recruited to laser-induced DSBs (Figs. 7B-E). The kinetics of EWSR1-FLI1's DSB recruitment were delayed compared to native EWSR1, whose rapid recruitment is attributed to C-terminal, positively charged arginine-glycine-glycine (RGG)-rich domains not present in EWSR1-FLI1 (Figs. 7A-E). To test how loss of these RGG domains impact DSB recruitment of EWSR1-FLI1, we reintroduced either 1 or all 3 RGG-rich domains (the entire EWSR1 C-terminus) into the fusion oncoprotein. In an RGG dose-dependent manner, the RGG containing versions of EWSR1-FLI1 displayed earlier DSB recruitment kinetics and higher levels of overall recruitment when compared to EWSR1-FLI1 (Fig. S7A, B). Moreover, the full (3) RGG domain containing version of EWSR1-FLI1 further reduced EWSR1 recruitment to laser-induced DSBs (and ATM signaling) beyond the effects seen with EWSR1-FLI1 (Figs. S7C-F), providing additional support for an interference/competition model between EWSR1-FLI1 and native EWSR1 at DSB sites.

Importantly, EWSR1-FLI1 recruitment to DSBs represents an unanticipated neomorphic property of the fusion protein contributed by the N-terminal intrinsically disordered region (IDR) of EWSR1. Control experiments with the full-length FLI1 protein showed no accumulation at laser-induced DSBs (Fig. S7G). Consistent with the N-terminus of EWSR1 mediating DSB recruitment, mutation

of the DNA binding domain of FLI1 (R2L2 mutant of EWSR1-FLI1[65]) had no effect on the DSB localization of EWSR1-FLI1 (Fig. S7H). Lastly, knockdown of native EWSR1 reduced accumulation of EWSR1-FLI1 at laser-induced DSB stripes, indicating that the localization of EWSR1-FLI1 to DSBs depends, at least in part, on native EWSR1 (Fig. S7I).

We tested the generality of the concept that N-terminal IDRs, as a shared structural feature of FET fusion oncoproteins (Fig. 7A), could promote aberrant DSB recruitment in other tumors within this class. EWSR1-ATF1 is the sole oncogenic driver of clear cell sarcoma (CCS) and contains the identical N-terminal IDR sequence as EWSR1-FLI1. The EWSR1-ATF1 fusion oncoprotein localized to laser-induced DSBs with delayed recruitment kinetics similar to EWSR1-FLI1, though with differences in departure timing (Figs. 7F, G). Like EWSR1-FLI1, reintroduction of either 1 or all 3 RGG-rich domains into EWSR1-ATF1 resulted in earlier DSB recruitment kinetics and higher levels of overall recruitment in an RGG dose-dependent manner (Fig. S7J).

Analogous to our findings in ES, CCS cells are dependent on HR factors PALB2 and BRCA1 for survival (Fig. S7K, L). Moreover, transient knockdown of EWSR1-ATF1 in a patient-derived CCS cell line increased downstream ATM signaling (phosphorylation of ATM targets CHK2 and KAP1) in response to IR, with either no effect (DNA-PK) or slight decrease (ATR) in activation of the other upstream DDR kinases (Figs. 7H, I and S7M, N). These data also reveal differences between FET fusion oncoproteins; only EWSR1-FLI1 affected the initial activation of ATM (autophosphorylation), while both EWSR1-ATF1 and EWSR1-FLI1 caused functional ATM defects in terms of downstream signaling. Despite these differences, the consequence of functional ATM defects in CCS was similarly increased reliance on compensatory ATR signaling, as CCS cells displayed EWSR1-ATF1-dependent, nanomolar range sensitivity (IC50: 27nM) to ATR inhibitor treatment with elimusertib (Fig. 7J). Taken together, our results support a model in which EWSR1 fusion oncoproteins are aberrantly recruited to DSB repair sites and induce specific defects in ATM function.

Anti-tumor activity of ATR inhibitor elimusertib across FET rearranged PDX models

Lastly, we tested ATR inhibition as a therapeutic strategy in FET fusion oncoprotein-driven cancers. We hypothesized that the ATM/ATR synthetic lethality seen in ATM mutant (loss of function) cancers[49-51] might extend to FET rearranged tumors with functional ATM defects caused by the FET fusion oncoproteins themselves. First, we determined whether FET fusion oncoprotein-driven cancer cell lines display increased sensitivity to the ATR inhibitor elimusertib that is currently being tested in multiple early phase clinical trials[66]. Our panel included 4 ES cell lines with varying TP53 and STAG2 status (see Supplementary Note 2), 1 CCS (EWSR1-ATF1), 2 desmoplastic small round cell tumor (EWSR1-WT1), and 1 myxoid liposarcoma cell line (FUS-CHOP), and multiple non-FET rearranged cancer cell lines as controls. FET fusion-driven cancer cell lines were significantly more sensitive to ATR inhibitor treatment than the control cell lines tested with IC50's between 20-60 nM (Fig. 8A), comparable to previously reported elimusertib IC50's for ATM mutant cancer cell lines[67]. To test our hypothesis in a larger unselected panel of cancer cell lines, we utilized DepMap screening data for elimusertib in 880 cancer cell lines which includes 17 ES samples. ES cell lines were again significantly more sensitive to ATR inhibition than the larger cohort of cancer cell lines (Fig. 8B), though our data does not exclude alternate mechanisms of sensitivity to ATR inhibition such as ATM and other DDR gene mutations as previously reported[51].

We then tested whether the observed in vitro sensitivity to ATR inhibition would translate to in vivo patient-derived xenograft (PDX) models of FET rearranged cancers. Elimusertib was tested in 5 PDX models: 2 ES models (ES-1 from initial diagnosis and ES-2 from a multiply relapsed patient), 2 CCS models (CCS-1 from initial diagnosis and CCS-2 from relapsed disease), and 1 desmoplastic small round cell tumor (DSRCT) PDX derived from a post-treatment surgical resection, for which we also verified that the DSRCT fusion EWSR1-WT1 is recruited to laser-induced DSBs with similar kinetics to EWSR1-FLI and EWSR1-ATF1 (Figs. S8A, B). Clinical

details on the tumor models are provided in Supplementary Table 3. Elimusertib was dosed at 40 mg/kg twice daily per oral gavage, on a 3 days-on/4 days-off schedule until tumors exceeded prespecified size endpoints as previously described[67]. There was minimal toxicity associated with this treatment regimen as assessed by weights and general activity scores, suggesting good tolerability of this dosing schedule.

Single-agent ATR inhibitor treatment significantly decreased tumor growth and increased progression-free survival in all 5 PDX models including those derived from relapsed ES and CCS patients (Figs. 8C-G). The DSRCT xenograft showed the best response (partial by RECIST criteria, >50% reduction in tumor volume, Fig. 8E). Interestingly, the ES-1 and CCS-1 PDX models from initial diagnosis showed prolonged stable disease (18 days of stable disease compared to immediate progression in vehicle treated tumors at day 4) and better overall response to elimusertib than the ES-2 and CCS-2 PDXs derived from relapsed disease, though testing of additional ES and CCS PDX models will be important to clarify whether PDX's derived from diagnostic and relapsed disease have differential responses to ATR inhibition.

To identify pharmacodynamic markers of elimusertib activity, we performed immunohistochemistry (IHC) for Ki-67 (cell proliferation), cleaved caspase-3 (apoptosis), and DNA damage (gH2AX). We observed decreased Ki-67 in elimusertib treated tumors compared to vehicle controls reflecting decreased proliferation, while increased cleaved-caspase 3 was only observed in the 2 ES PDXs (Figs. S8C-F). Consistent with prior reports[68,69], we were unable to validate a direct biomarker of ATR inhibition as p-ATR could not reliably be assessed by IHC and its downstream target p-CHK1 did not show a significant difference between vehicle and elimusertib treatment (Figs. S8C-F), which may reflect the low-level of ATR pathway activation at baseline. However, gH2AX proved to be a reliable biomarker for elimusertib activity. The fraction of gH2AX positive cells was significantly increased in all elimusertib treated tumors compared to vehicle controls, consistent with unrepaired and ongoing DNA damage as the mechanism of cell

death and anti-tumor activity. Taken together, our data demonstrate that FET rearranged cancers are preferentially sensitive to ATR inhibition and that single agent treatment with the ATR inhibitor elimusertib has in vivo anti-tumor activity across multiple FET fusion oncoprotein-driven PDX models.

Discussion

Here we describe how an oncogene can functionally interfere with tumor suppressive DNA damage repair networks and reveal a new mechanism: aberrant recruitment of an oncogenic fusion protein to sites of DNA damage causing disruption of the physiologic DDR. As a consequence of aberrant recruitment, we identify functional ATM defects as a principal DNA repair lesion in ES and demonstrate oncogene-dependent synthetic lethality with ATR inhibition as a collateral dependency in multiple FET rearranged cancers. These data provide a template for the broader utilization of DDR-directed therapies in cancer through improved understanding of oncogene-DDR network interactions. More generally, our findings provide initial examples of how an oncogene can impair physiologic DNA repair to create functional states akin to genetic DDR pathway loss (e.g., ATM tumor suppressor mutations).

The nature of the DNA repair defect in ES has been the subject of much debate based on the strong clinical and laboratory-based data demonstrating chemo- and radio-sensitivity[11-15]. Our discovery that ES tumors are not “BRCA-like”, but instead harbor functional ATM defects, may help explain the lack of clinical responses to PARP inhibitor monotherapy in ES patients[16,70] (unlike HR deficient BRCA mutant and BRCA-like cancers[17,18]). ES cells are dependent on key HR genes for survival and direct analysis of ES patient tumors revealed none of the genomic hallmarks of HR loss. Instead of isolated HR deficiency, we show that EWSR1-FLI1 creates a broader defect in resection-dependent DSB repair and a specific impairment of upstream ATM activation and signaling. The observed ATM defects do not appear to depend on TP53 or STAG2

status as the phenotypes were observed in both mutant and wild-type ES cell lines (see Supplemental Note 2), though we do not exclude possible contributions and that TP53 and STAG2 status may have important downstream consequences for cell viability[71], metastatic potential[72], and clinical outcomes in patients[34,73] as previously described.

To contextualize the magnitude of ATM defects reported here, we benchmarked EWSR1-FLI1 against loss of canonical ATM activators. The effect size of EWSR1-FLI1 mediated suppression of ATM activation/signaling is comparable to loss of established ATM activators including MDC1, RNF8 or RNF168, but only ~30-60% of the near-complete functional ATM deficiency seen with loss of the MRN complex. Thus, the ATM defects reported here are biologically significant, but not absolute. We demonstrate the functional importance and therapeutic relevance of (partial) ATM suppression through increased reliance on a compensatory DDR kinase, ATR, and EWSR1-FLI1-dependent synthetic lethality with ATR inhibitors. These data nominate functional ATM defects as a principal DNA repair lesion in ES.

How does EWSR1-FLI1, a TF fusion oncoprotein, create these DNA repair defects in ES? We did not identify a set of EWSR1-FLI1 transcriptional targets to explain these effects (e.g., MRN complex genes were not suppressed nor absent as assayed by cell line proteomics). Instead, we discovered that EWSR1-FLI1 is aberrantly recruited to DNA DSBs through homotypic intrinsically disordered domain (IDR) interactions with native EWSR1 and causes premature loss of native EWSR1 from DSB sites. Our finding that knockdown of native EWSR1 largely phenocopies the DNA repair defects caused by EWSR1-FLI1 implicates the interaction between shared N-terminal IDRs of EWSR1/EWSR1-FLI1 and loss of EWSR1 function as central to the DNA repair defects in ES. Our work raises important new questions about the biology of native FET proteins and how IDR-mediated phase separation enables DSB compartmentalization and coordinates subsequent repair.

There are also differences between the DNA repair phenotypes observed when comparing loss of EWSR1 with EWSR1-FLI1 expression, most notably the opposite effects on canonical NHEJ (cNHEJ). In our model (Fig. 9), we propose that early RGG-dependent DSB recruitment of native FET proteins mediates fast cNHEJ repair (consistent with prior reports on FUS[22,74]). Thus, despite EWSR1-FLI1 expression in ES, the preserved early recruitment kinetics of native EWSR1 (Fig. 6B) still allows robust cNHEJ (in contrast to EWSR1 knockdown in non-ES cells). The extent to which the hemizygosity of native EWSR1 in ES tumors contributes to DNA repair phenotypes and how aberrant recruitment of an ordered TF domain (e.g., FLI1) might disrupt DSB compartmentalization and subsequent repair are a set of new mechanistic questions that emerge from our findings.

More generally, the shared structural organization across the class of FET fusion oncoproteins (i.e., retention of N-terminal IDRs that mediate homotypic and heterotypic FET protein interactions and loss of C-terminal RGG domains that promote rapid DSB recruitment, Fig. 7A) raised the intriguing hypothesis that FET fusion-driven cancers harbor a common set of DNA repair defects. Indeed, our finding that the clear cell sarcoma fusion oncoprotein EWSR1-ATF1 localizes to DNA DSBs and induces similar functional ATM defects (though with differences in ATM autophosphorylation, Fig. 7H) supports a more general role for FET fusion oncoproteins in regulating and disrupting DNA DSB repair. Analogous to our findings in ES, CCS cells also display FET fusion oncogene-dependent nanomolar range sensitivity to the ATR inhibitor elimusertib. These data prompted us to test ATR inhibition across the class of FET rearranged cancers as a synthetic lethal therapeutic strategy to specifically target functional ATM defects induced by FET fusion oncoproteins.

We selected a potent ATR inhibitor in clinical development (elimusertib) and observed nanomolar range IC50's and preferential sensitivity of FET fusion-driven cancer cell lines in vitro (IC50 range: 20-60nM), comparable to reported elimusertib IC50's in cell lines with pathogenic loss of function

ATM mutations[67]. Moreover, we tested single agent elimusertib treatment in 5 PDX models including 2 ES, 2 CCS, and 1 Desmoplastic small round cell tumor (DSRCT) model. All 5 models showed significant decreases in tumor growth and prolongation of progression-free survival including ES and CCS PDXs from multiply relapsed patients. Given that PDXs are a stringent bar in terms of disease control due to their inherent heterogeneity and single agents are highly unlikely to be curative for these set of diseases, the ability of ATR inhibitor monotherapy to control tumor growth in all 5 models was a striking finding. Our findings are consistent with published reports testing elimusertib in pediatric cancer PDX's (ES was the only FET rearranged tumor tested)[75], but differ from a recent report with another ATR inhibitor in clinical trials (berzosertib) that showed no anti-tumor activity as monotherapy in ES cell line xenografts[76], suggesting important potential differences between ATR inhibitors that warrant future study. We note that previously described mechanisms of ATR inhibitor sensitivity such as PGBD5 transposase expression[77] or replication stress[15] could also contribute to the elimusertib effects that we observed. In total, these data provide strong preclinical rationale for specifically testing elimusertib (and combinations thereof) in FET rearranged cancers as part of ongoing early phase clinical trials.

Finally, what might be the selective advantage for an oncogene to also induce a DNA repair defect? We propose that by partially disabling physiologic DDR signaling, cells with FET fusion oncoproteins can tolerate high levels of DDR activation caused by transcription and replication stress induced by the oncoprotein itself and thus overcome an important barrier to cellular transformation. Whether other TF fusion oncoproteins (or oncogenes more generally) interact with and disrupt tumor suppressive DDR signaling networks as part of oncogenesis will be an intriguing topic for future work. In summary, our study provides a new mechanism for how oncogenes interact with DNA repair networks to disrupt physiologic DNA DSB repair, and rationale for a new targeted therapeutic strategy (i.e., ATM/ATR synthetic lethality) in ES and the broader class of undruggable FET fusion-driven cancers.

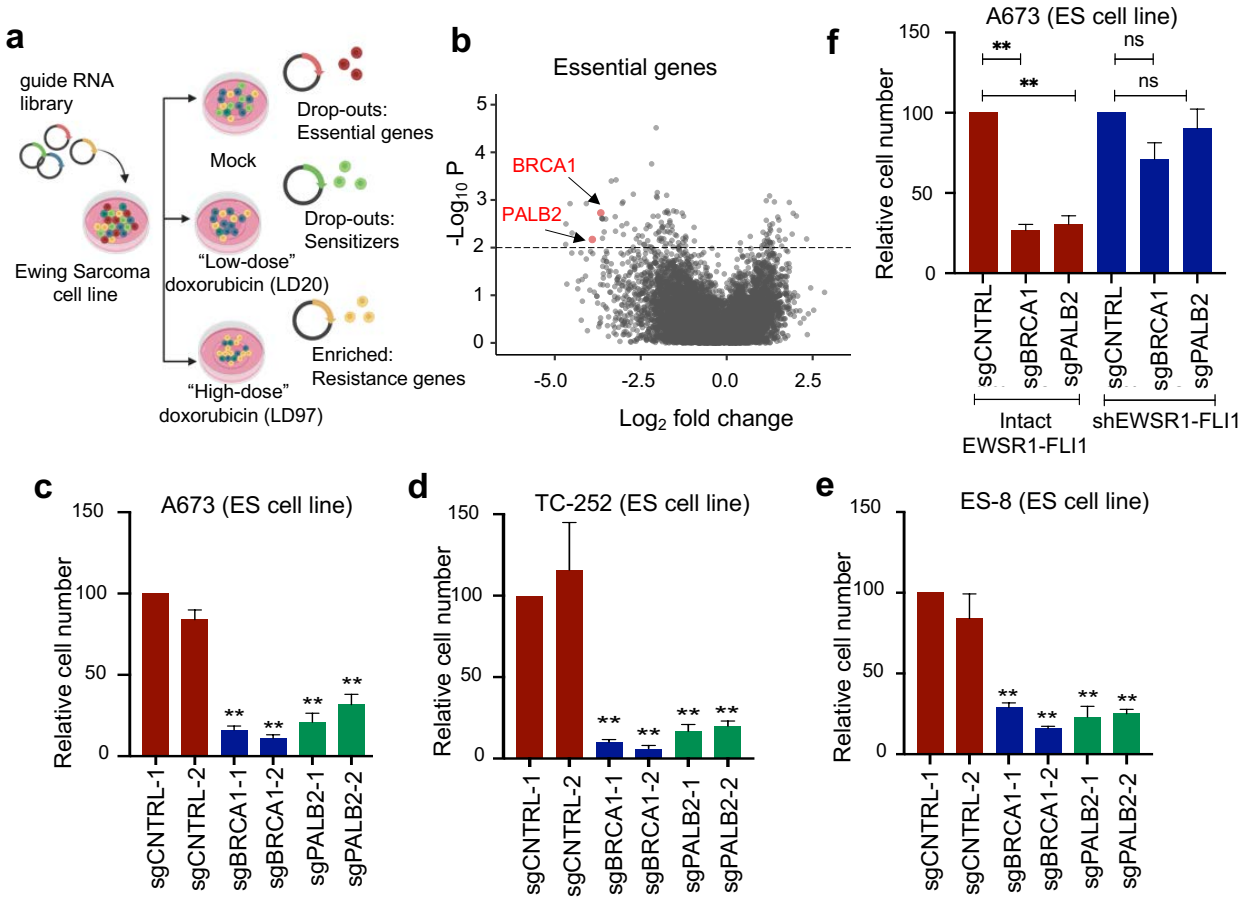

Figure 1: ES cells are dependent on HR factors for survival.

A) Schematic of CRISPRi genetic screen of 7,000 cancer associated genes in ES cell line A673.

B) Volcano plot of sgRNA log_2fold change (X-axis) vs -log10(p value), average of 2 biologic replicates. Full screen results in Supplementary Table 1.

C-E) Growth assays in dCas9 expressing ES cell lines upon introduction of 2 independent sgRNAs against BRCA1, PALB2, or control. n = 4.

F) Growth assays in ES cell line A673 with doxycycline-inducible shRNA against EWSR1-FLI1.

For all panels, error bars represent ± SEM, $^{**}p < 0.01$ by one-way ANOVA with post hoc Tukey's HSD test.

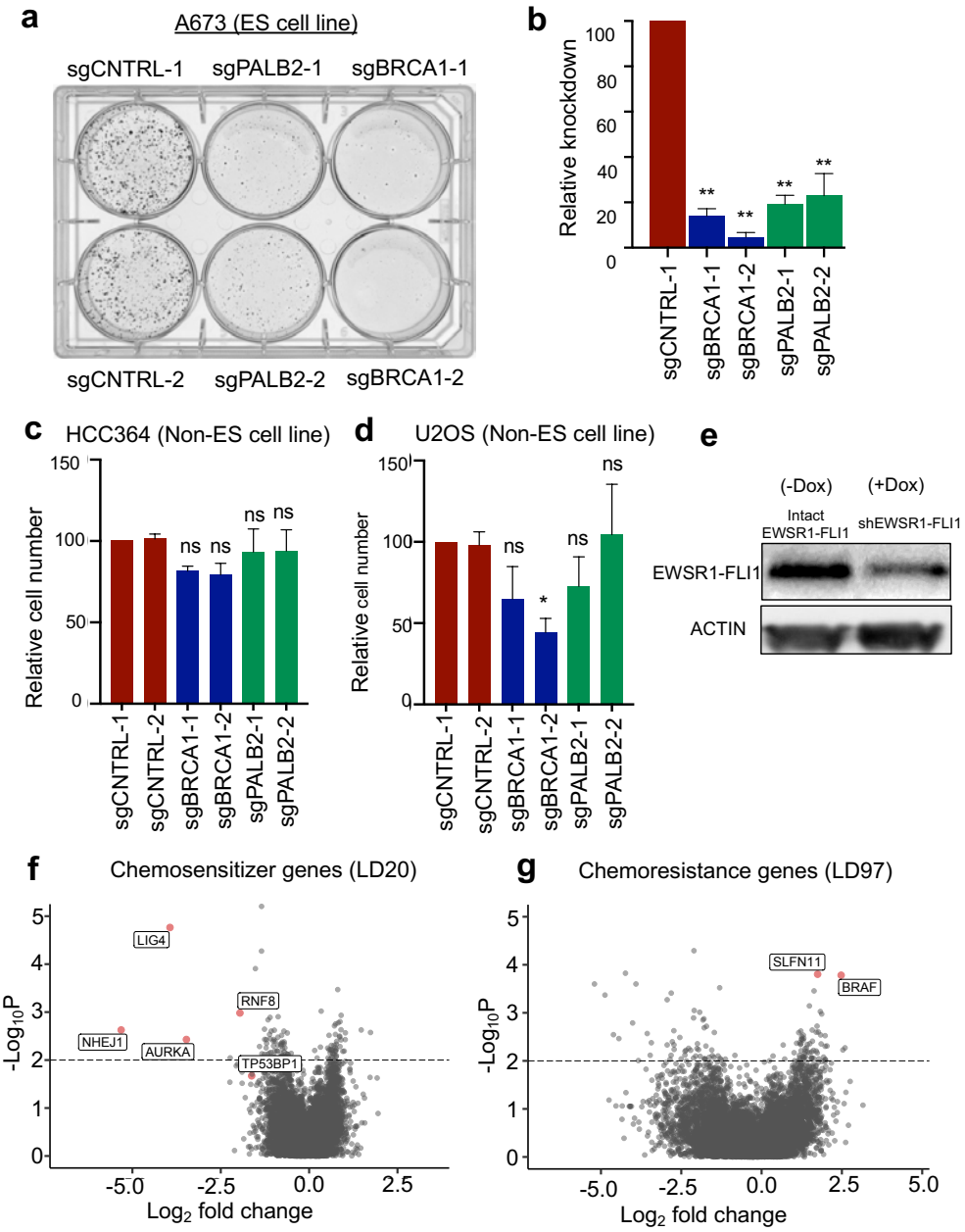

Supplemental Figure 1: ES cells are dependent on HR factors for survival.

A) Representative crystal violet staining of 72-hour growth assay in dCas9 expressing A673 ES cells upon introduction of 2 independent sgRNAs against BRCA1, PALB2, or control.

B) Relative knockdown of each sgRNA by qPCR, n = 3.

C, D) Growth assays in dCas9 expressing cancer cell lines upon introduction of 2 independent sgRNAs against BRCA1, PALB2, or control, n = 4, 4.

E) Western blot of EWSR1-FLI1 levels in A673 with doxycycline-inducible shRNA against EWSR1-FLI1.

F, G) Volcano plot of sgRNA $\log_2$fold change relative to DMSO control (X-axis) vs -log10(p value). Full screen results provided in Supplementary Table 1.

For all panels, * denotes p< 0.05, ** denotes p < 0.01, ns denote not significant by one-way ANOVA with post hoc Tukey's HSD test.

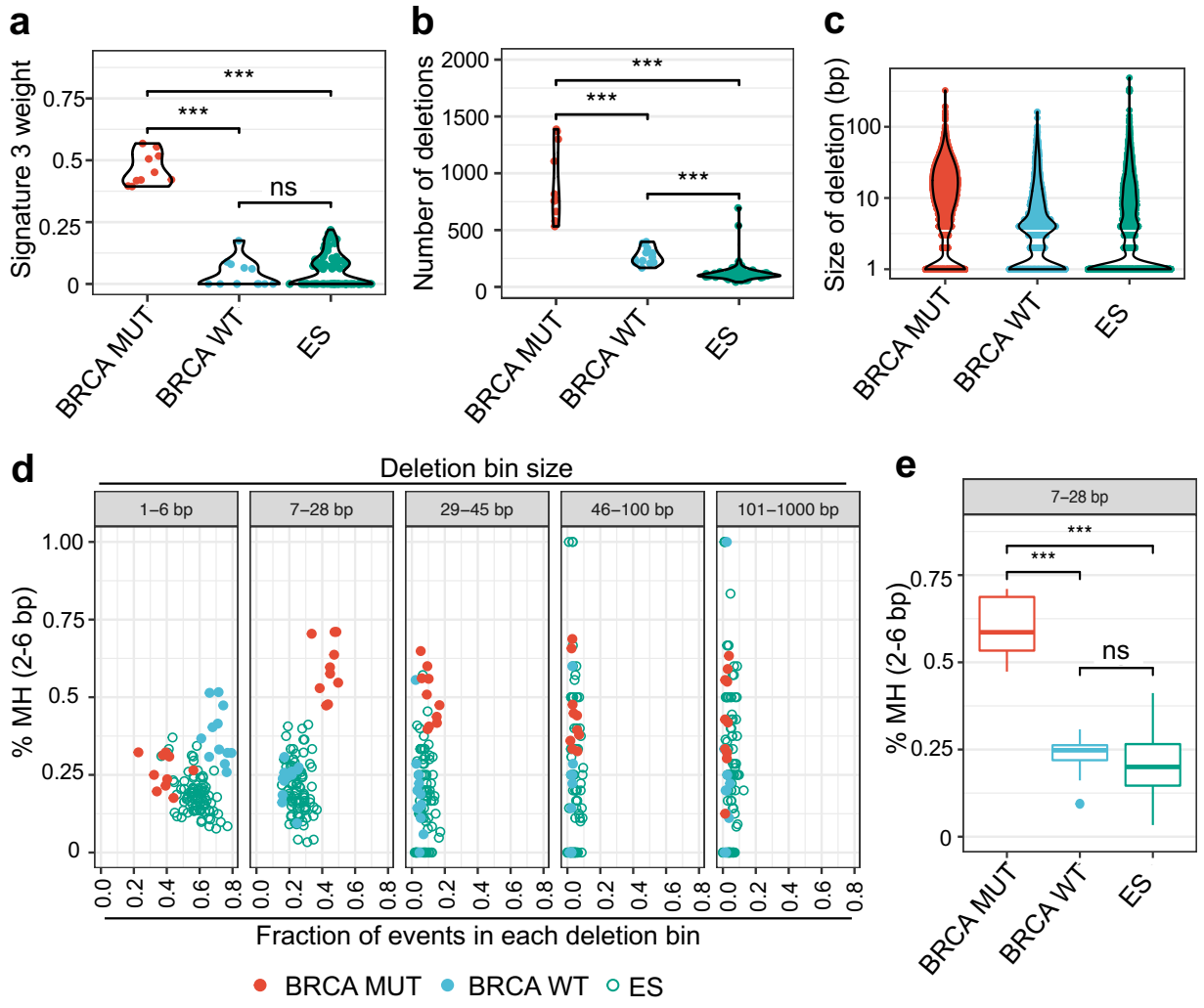

Figure 2: ES patient tumors do not display the genomic scars of HR deficiency.
A) Weight of mutational signature 3 shown for BRCA mutant, wild-type, and ES tumor samples.
B) Total number of unique deletions per sample.
C) Size of MuTect deletions compared across tumor groups.
D) For all samples, deletions were first subdivided into specific base pair (bp) length bins, then the fraction of deletions with 2-6bp microhomology (MH) was plotted (Y-axis) vs. the fraction of deletions present in this bin (X-axis).
E) Breakout of the 7-28bp deletion length bin showing the distribution of deletions with microhomology (2-6bp).
For all panels, *** denotes p< 0.001, ns denotes not significant by Mann-Whitney test. European Genome-phenome Archive accession numbers: ES samples (EGAS00001000855 - Institute Curie cohort and EGAS00001000839 - St. Jude's cohort)[34], breast cancer samples (EGAD00001001322)[35].

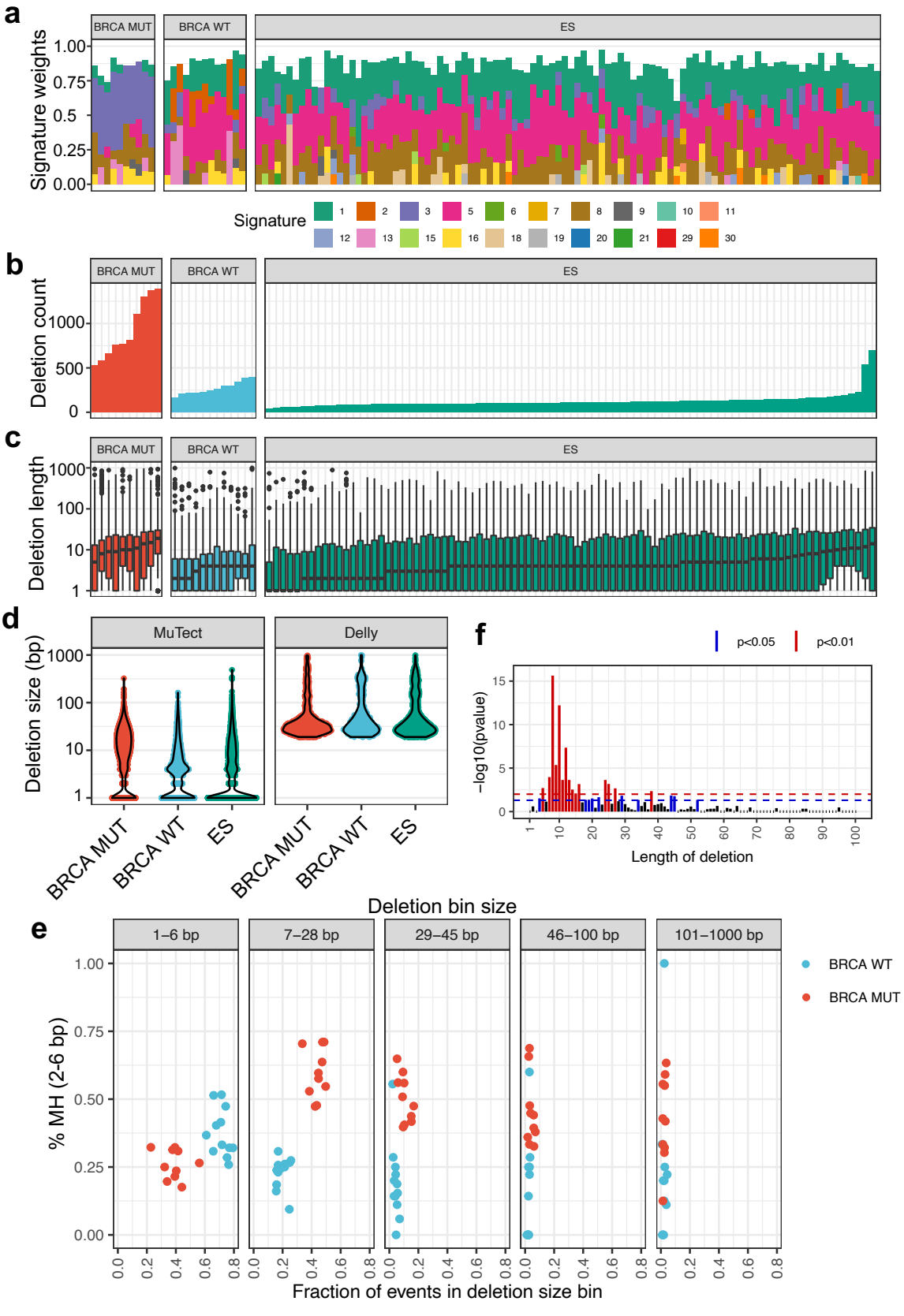

Supplemental Figure 2 continues on next page

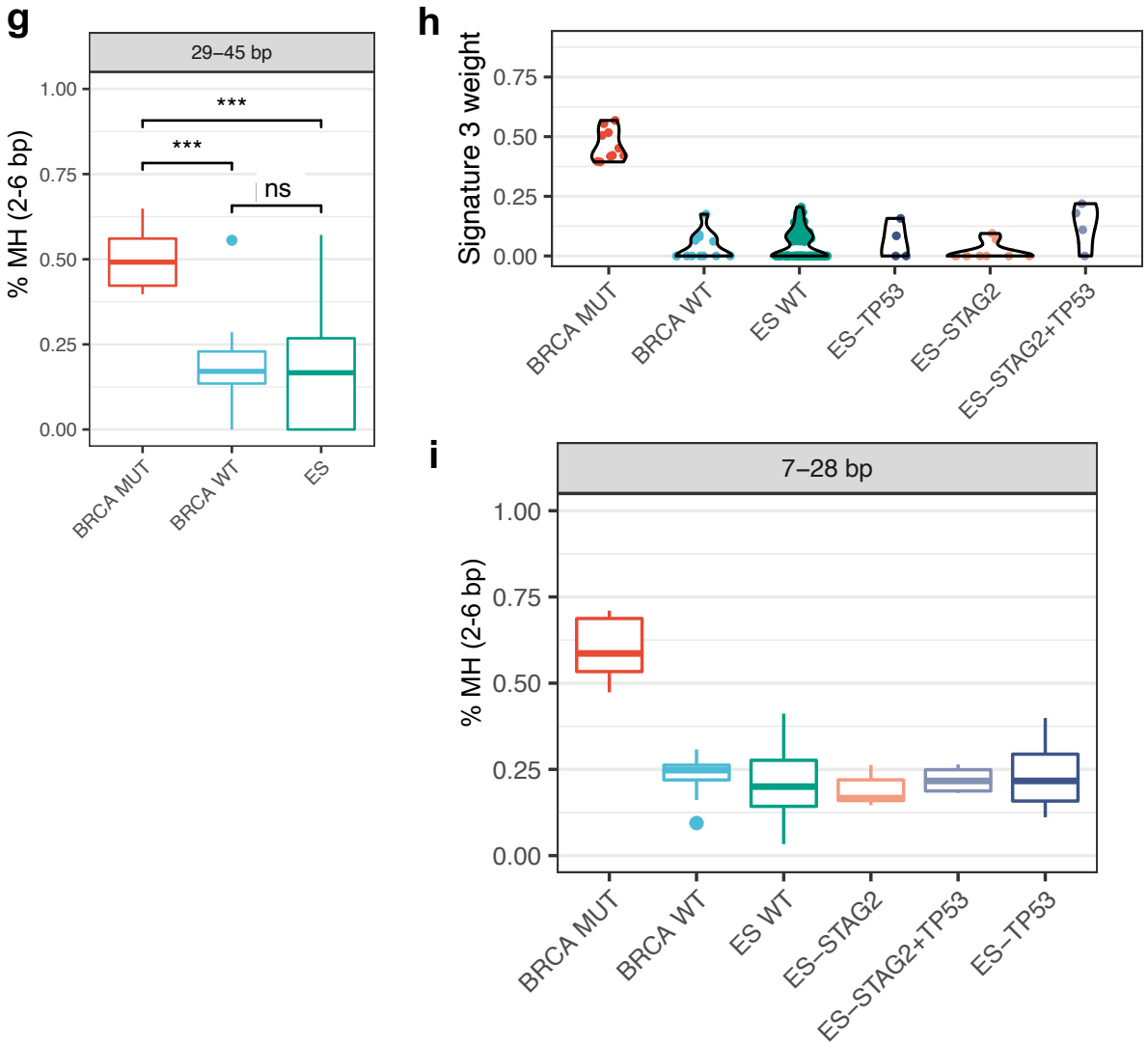

Supplemental Figure 2: ES patient tumors do not display the genomic scars of HR deficiency.

A) Mutational signature breakdown for BRCA mutant (MUT)/wild-type (WT) and ES tumors.
B) Total number of unique deletions per sample.
C) Deletion length per sample.
D) Deletion size per tumor sample shown individually for MuTect and Delly deletion calls.
E) Deletion size/microhomology (MH) profile for only BRCA WT and BRCA MUT samples showing separation between the groups present in the 7-28bp and 29-45bp bins in both the fraction of events in deletion size bin (X-axis) and percentage of MH (Y-axis).
F) Graph of Fisher test significance (p value) for deletion lengths and MH status.
G) Breakout of the 29-45 base pair (bp) deletion length bin showing the fraction of deletions with 2-6 bp microhomology.
H, I) Signature 3 weight (H) and 2-6bp breakpoint MH in the 7-28bp deletion bin (I) in ES samples subdivided by TP53 and STAG2 mutational status. ES WT are wild-type for p53 and STAG2.
For all panels, *** denotes $p < 0.001$ by Mann-Whitney test, ns denotes not significant. European Genome-phenome Archive accession numbers: ES samples (EGAS00001000855 - Institute Curie cohort and EGAS00001000839 - St. Jude's cohort)[34], breast cancer samples (EGAD00001001322)[35].

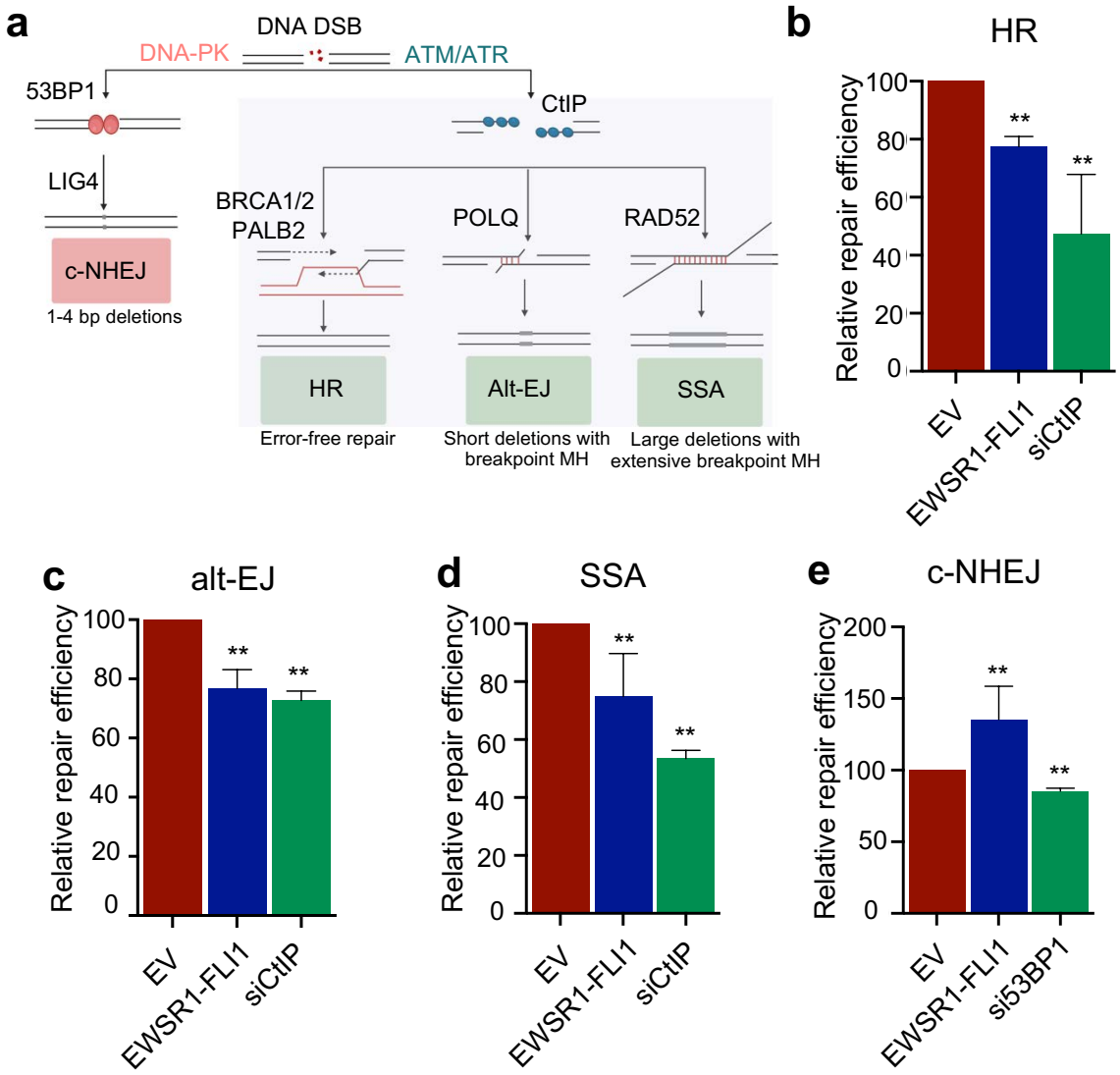

Main Figure 3: EWSR1-FLI1 impairs resection-dependent DSB repair.
A) Schematic of DSB repair. DSBs either undergo direct repair via c-NHEJ or bidirectional end-resection to create an intermediate for HR, alt-EJ, or SSA.
B-E) Relative repair efficiency as measured by GFP positivity in pathway-specific DSB repair reporters for HR (DR-GFP), alt-EJ (EJ2), SSA, and c-NHEJ (EJ5) upon expression of empty vector (EV), EWSR1-FLI1, or siRNA gene knockdown for 72 hours.
For all panels, error bars represent ± SEM, ** denotes $p < 0.01$ by one-way ANOVA with post hoc Tukey's HSD test. n=4 for all panels.

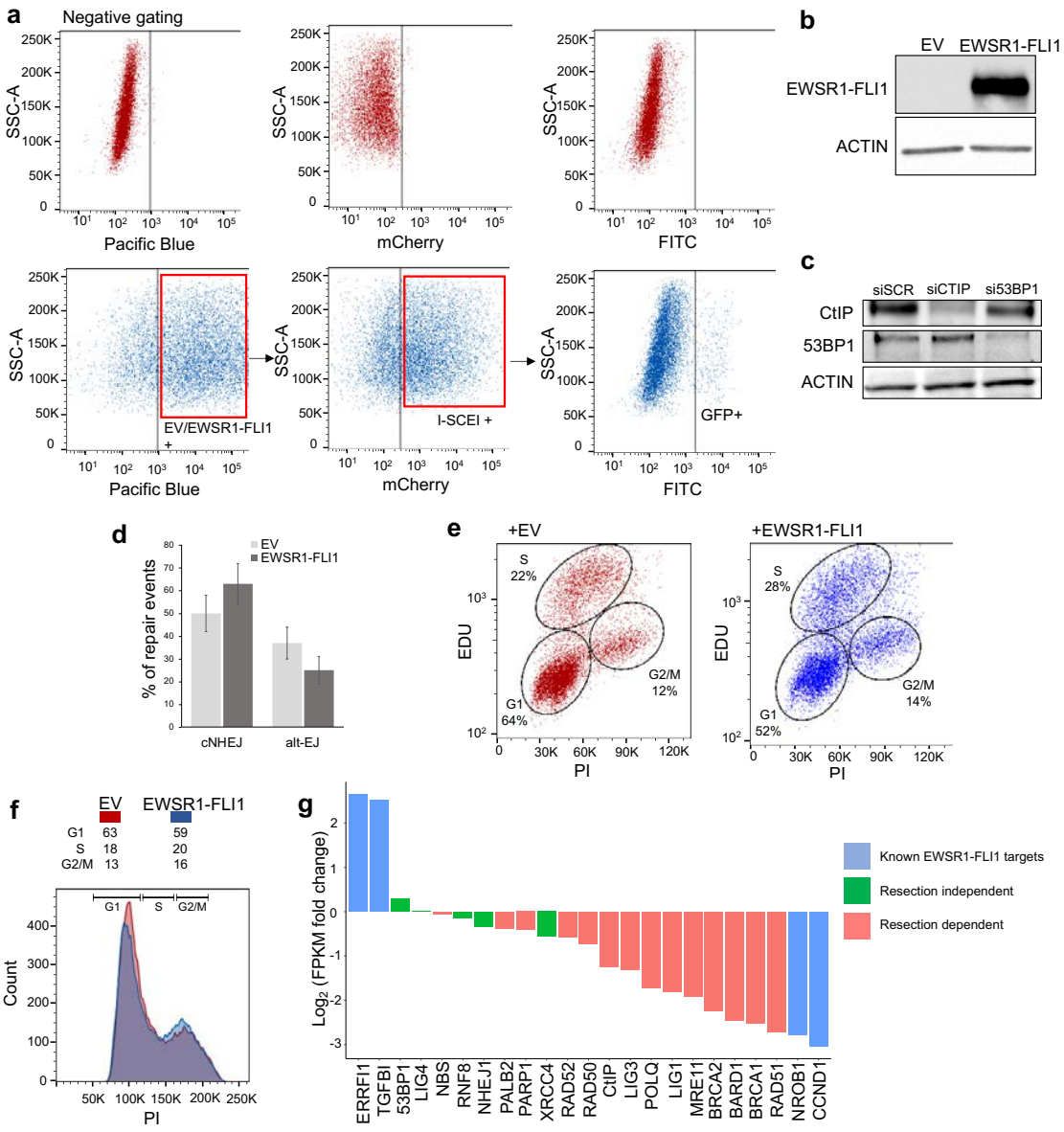

Supplemental Figure 3: EWSR1-FLI1 impairs resection-dependent DSB repair.

A) Gating schema for pathway-specific DSB repair reporter assays in U2OS cells using dual promoter vector expressing mTagBFP and EWSR1-FLI1 (or empty vector, EV), followed by introduction of mCherry-I-SceI endonuclease. GFP positivity is measured at 72 hours.

B) Representative Western blot showing EWSR1-FLI1 expression level in DSB repair reporter assays.

C) Western blot showing knockdown of relevant DSB repair genes.

D) Sequence analysis of repair events after transient introduction of I-SceI DSB reporter (NHEJ-I)[40] in U2OS cells expressing EV or EWSR1-FLI1. Error bars represent ± SEM, $p<0.05$ for both comparisons, paired t-test, n=3.

E) Cell cycle profiles using EdU incorporation in U2OS cells +/- EWSR1-FLI1.

F) Cell cycle profiles using Propidium Iodide (PI) +/- EWSR1-FLI1.

G) Analysis of published RNAseq data[41] in A673 (ES cells) with EWSR1-FLI1 knockdown. Blue denotes canonical EWSR1-FLI1 targets, red/green denotes resection-dependent and independent DNA repair genes respectively.

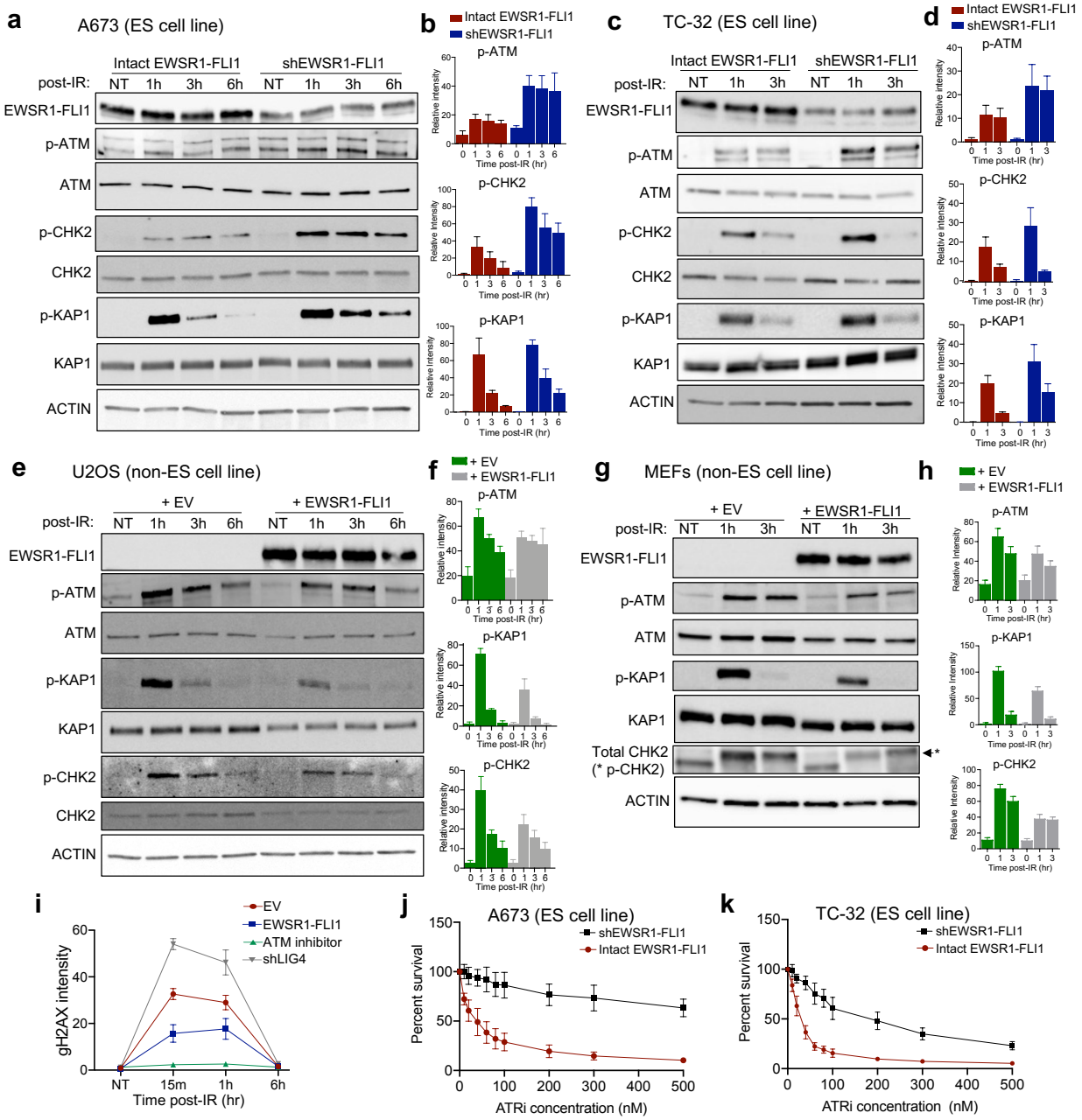

Main Figure 4: EWSR1-FLI1 impairs ATM activation and signaling.

A-D) Western blotting and quantification after IR (5 Gy) at indicated time points in ES cell lines (A673, TC-32) with doxycycline-inducible shRNA against EWSR1-FLI1.

E-H) Representative Western blots and quantification upon IR (5 Gy) at indicated time points in non-ES cell lines (U2OS, MEFs) upon expression of EV (empty vector) or EWSR1-FLI1.

I) gH2AX intensity by flow cytometry in non-ES (U2OS) cells post-IR (5 Gy) after expression of EV or EWSR1-FLI1. Control experiments with ATMi treatment (KU-55933, 1μM) or shRNA against Ligase IV (LIG4), $p < 0.05$ for all comparisons using one-way ANOVA with post hoc Tukey's HSD test.

J, K) ATR inhibitor (elimusertib) dose-response curves for ES cell lines A673 and TC-32 with dox-inducible shRNA against EWSR1-FLI1, $p<0.05$ for both comparisons, paired t-test.

For all panels, error bars represent ± SEM for at least 4 replicates for each panel.

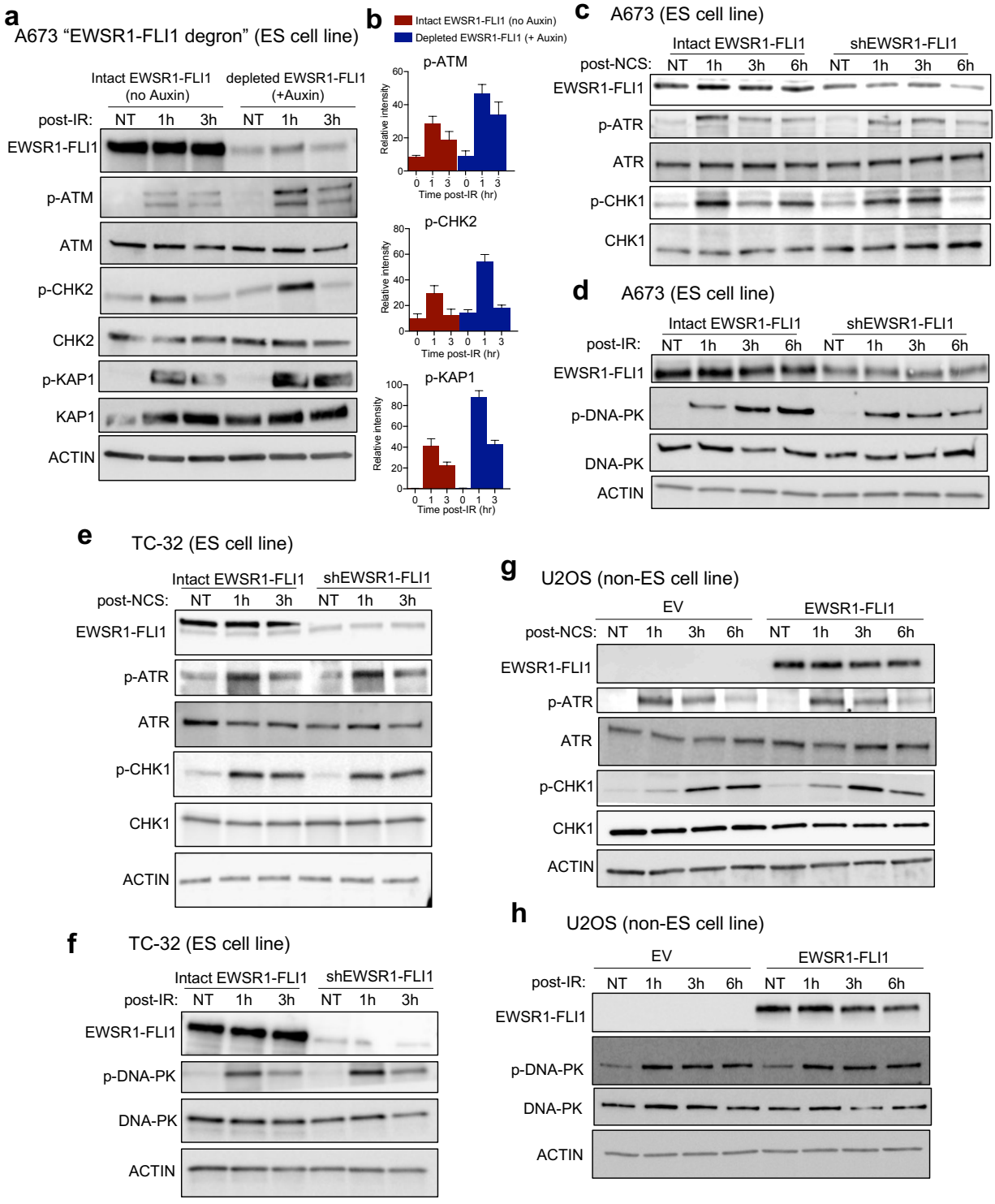

Supplemental Figure 4 continues on next page

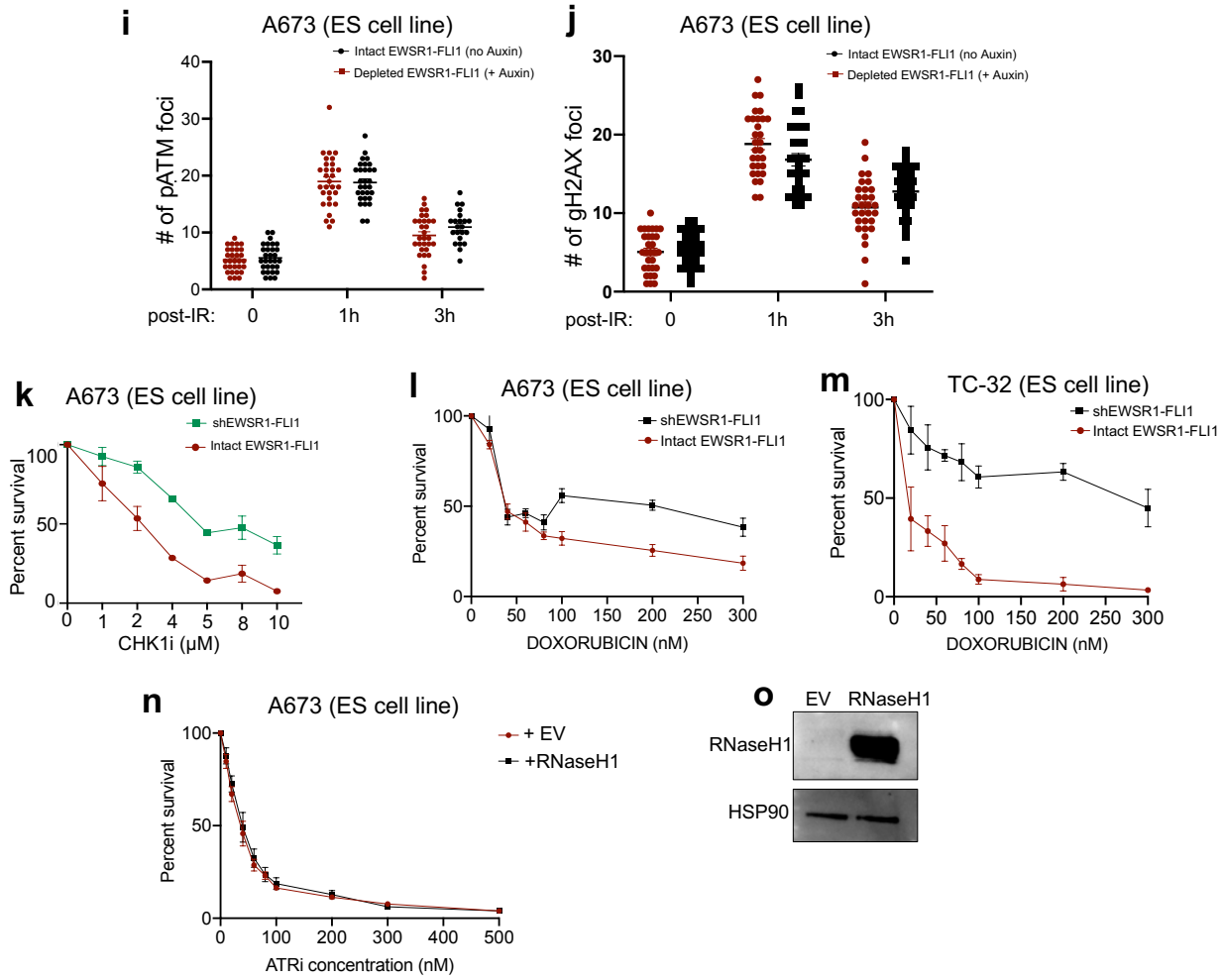

Supplemental Figure 4: EWSR1-FLI1 impairs ATM activation and signaling.

A, B) Western blotting and quantification upon 5 Gy IR at indicated time points in ES cell line A673 "EWSR1-FLI1 degron" +/- 200 μM IAA (auxin) for 3 hours to degrade endogenous EWSR1-FLI1.

C-H) Western blotting upon 200 ng/ml NCS treatment (C, E, G) or 5 Gy IR (D, F, H) at indicated time points in A673 and TC-32 ES cells with dox-inducible shRNA against EWSR1-FLI1 or upon EV or EWSR1-FLI1 expression in non-ES (U2OS) cancer cell line.

I, J) Quantification of p-ATM (I) and gH2AX foci (J) upon 5 Gy IR in A673 "EWSR1-FLI1 degron" ES cell line at indicated time points +/- addition of 200 μM IAA (auxin) for 3 hours to degrade endogenous EWSR1-FLI1.

K) CHK1 inhibitor dose-response curves in A673 with dox-inducible shRNA against EWSR1-FLI1, $p<0.05$ by paired t-test, n=3.

L, M) Doxorubicin dose-response curves for ES cell lines A673 and TC-32 with dox-inducible shRNA against EWSR1-FLI1, $p<0.05$ for both comparisons, paired t-test, n=3.

N, O) ATR inhibitor (elimusertib) dose-response curves for ES cell line A673 +/- RNAseH1 overexpression and confirmatory Western blot of RNAseH1 expression (K).

For all panels, error bars represent ± SEM and represent at least 3 replicates for each panel.

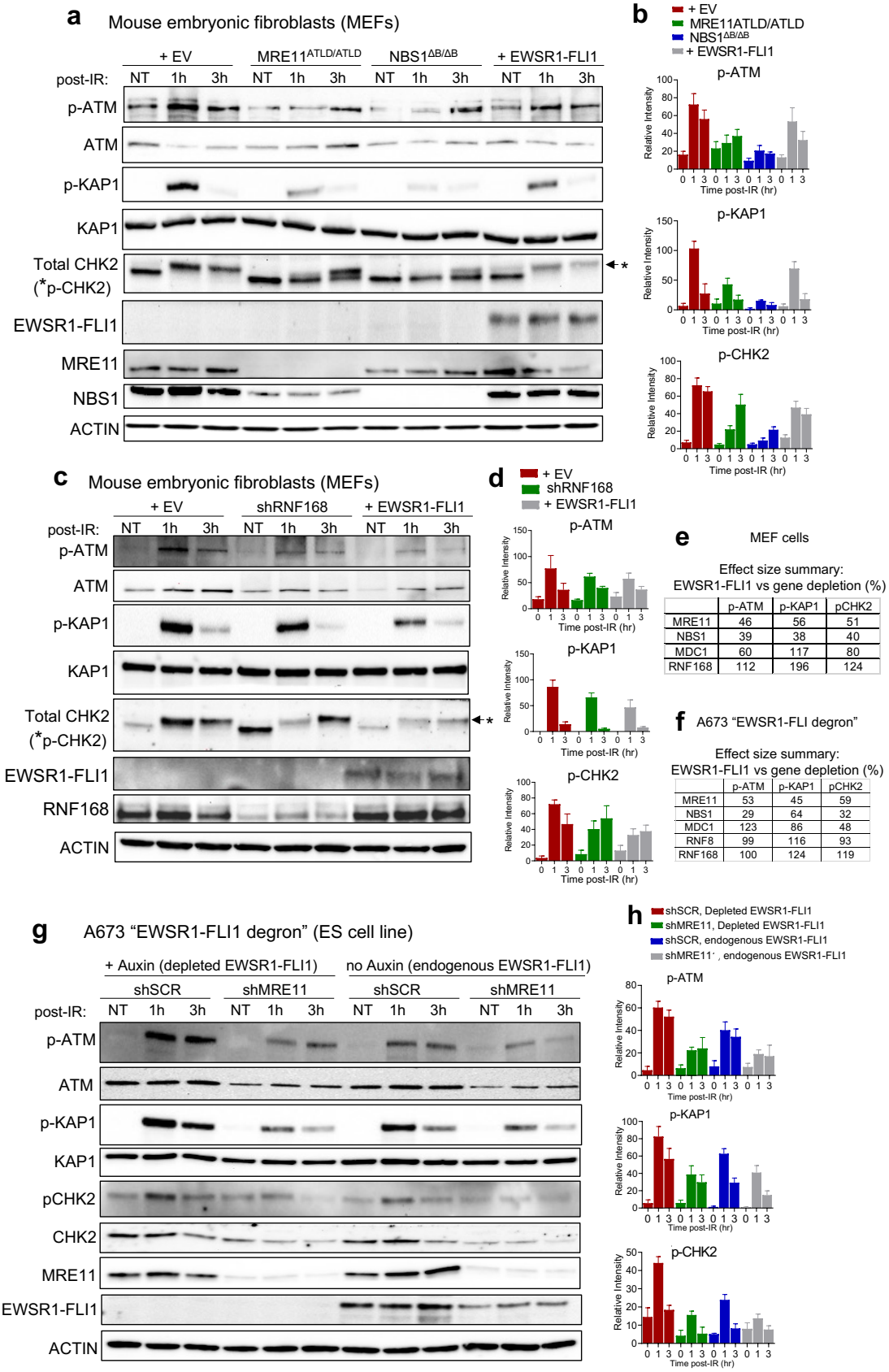

	p-ATM	p-KAP1	pCHK2
MRE11	46	56	51
NBS1	39	38	40
MDC1	60	117	80
RNF168	112	196	124

	p-ATM	p-KAP1	pCHK2
MRE11	53	45	59
NBS1	29	64	32
MDC1	123	86	48
RNF8	99	116	93
RNF168	100	124	119

(Figure 5 continues on next page)

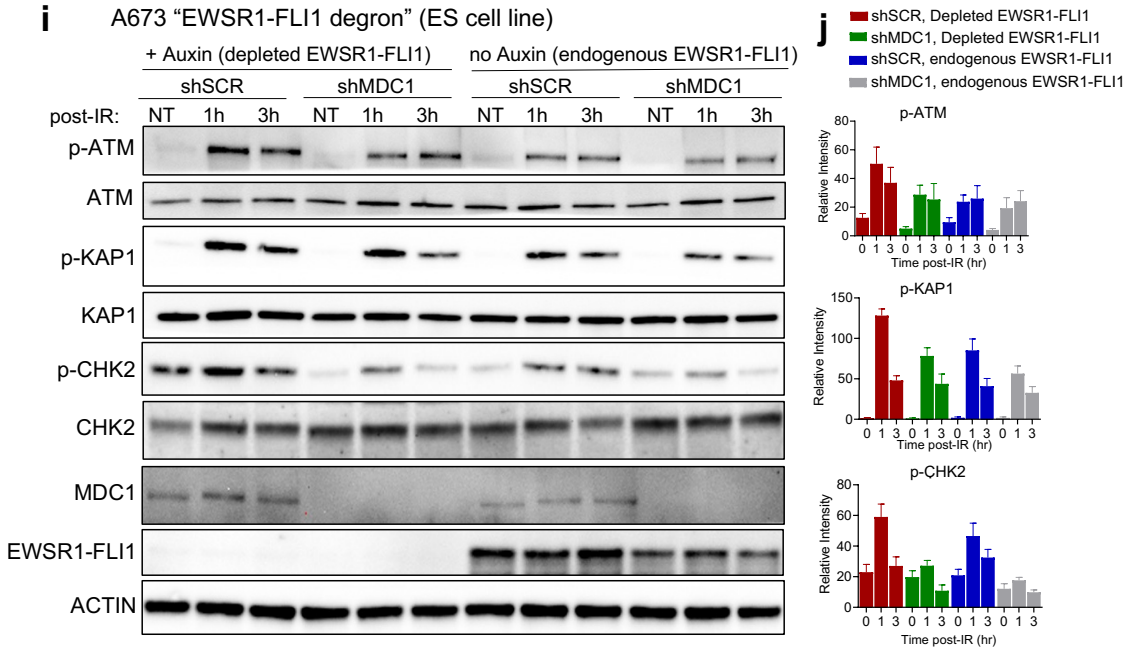

Main Figure 5: Comparison of EWSR1-FLI1 to loss of canonical ATM activators

A-D) Western blotting and quantification after IR (5 Gy) at indicated time points in either wild-type (WT) MEFs with empty vector (EV) or EWSR1-FLI1 expression, MRE11$^{ATLD/ATLD}$ and NBS1$^{\Delta B/\Delta B}$ MEFs (A, B), or WT MEFs with an shRNA against RNF168 (C, D).

E) Effect size comparison in MEFs of EWSR1-FLI1 to loss of ATM regulator in terms of ATM suppression (p-ATM/p-CHK2/p-KAP1) based on 1hr time point post-IR. % represents ratio of reduction from baseline (EV) of EWSR1-FLI1 vs. knockdown of ATM regulator.

F) Effect size comparison in A673 "EWSR1-FLI1 degron" cells of endogenous EWSR1-FLI1 to loss of ATM regulator in terms of ATM suppression based on 1hr time point post-IR. % represents a ratio of reduction from maximal ATM activity (gene knockdown, EWSR1-FLI1 depleted: red bars) for (1) shScramble (shSCR), endogenous EWSR1-FLI1 (blue bars) versus (2) gene knockdown, EWSR1-FLI1 depleted (green bars).

G-J) Western blotting and quantification upon 5 Gy IR at indicated time points in ES cell line A673 "EWSR1-FLI1 degron" infected with shRNAs against MRE11, MDC1, or shSCR. 200 μM IAA (auxin) added 3 hours prior to IR to degrade endogenous EWSR1-FLI1.

For all panels, error bars represent ± SEM and represent at least 3 replicates for each panel.

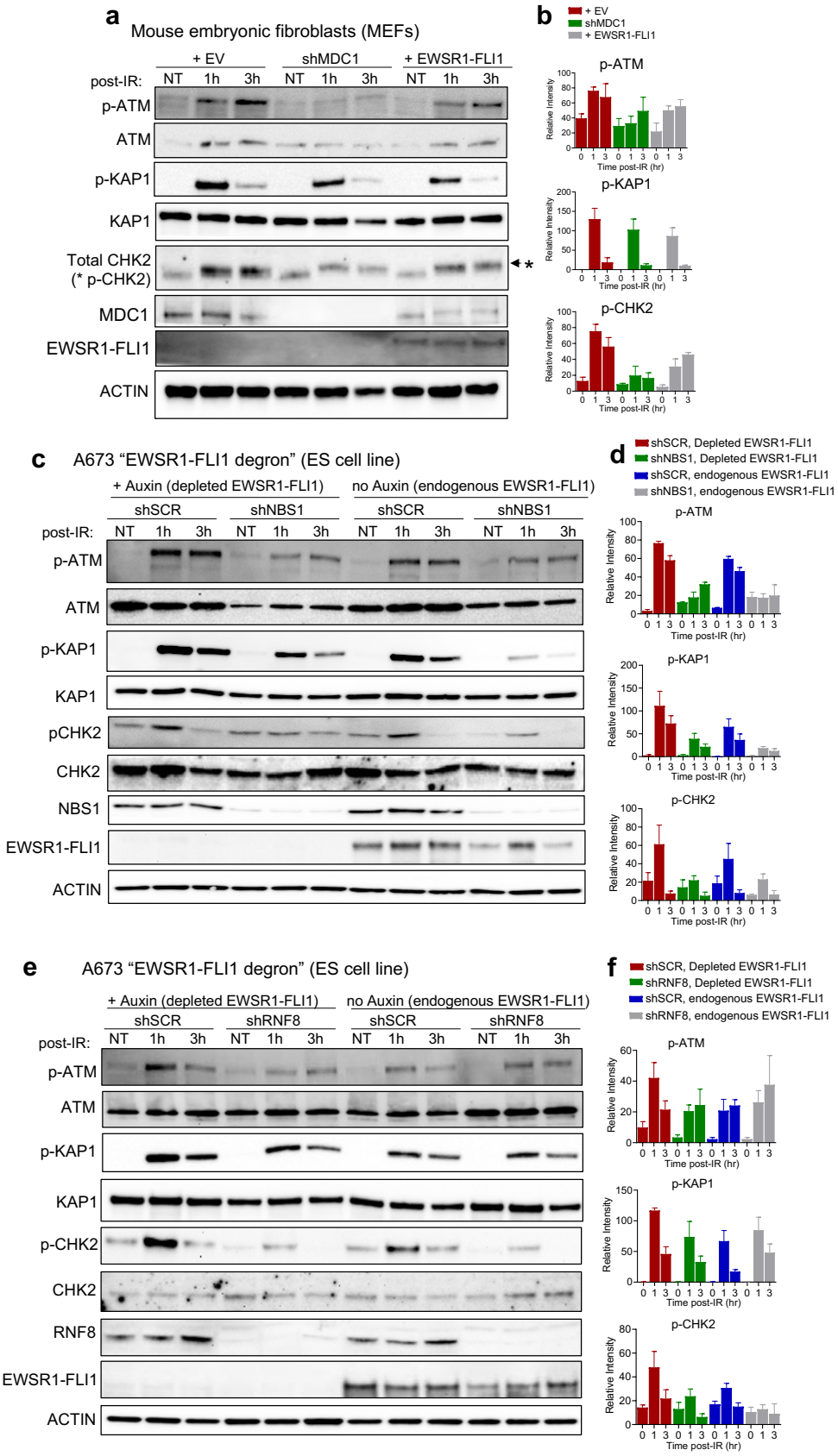

(Supplemental Figure 5 continues on next page)

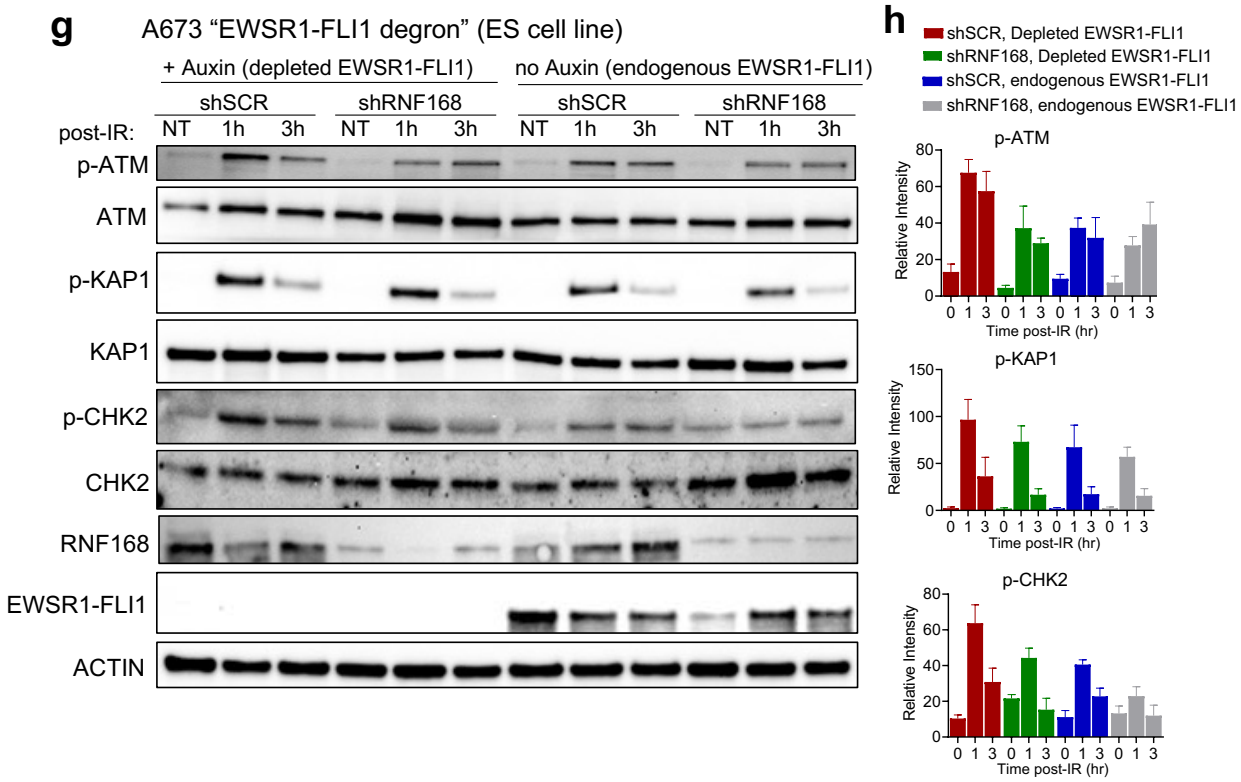

Supplemental Figure 5: Comparison of EWSR1-FLI1 to loss of canonical ATM activators
A, B) Western blotting and quantification after IR (5 Gy) at indicated time points in either wild-type (WT) MEFs infected with empty vector (EV), EWSR1-FLI1, or shRNA against MDC1.
C-H) Western blotting and quantification upon 5 Gy IR at indicated time points in ES cell line A673 "EWSR1-FLI1 degron" infected with shRNAs against NBS1, RNF8, RNF168, or shSCR. 200 μM IAA (auxin) added 3 hours prior to IR to degrade endogenous EWSR1-FLI1.
For all panels, error bars represent ± SEM and represent at least 3 replicates for each panel.

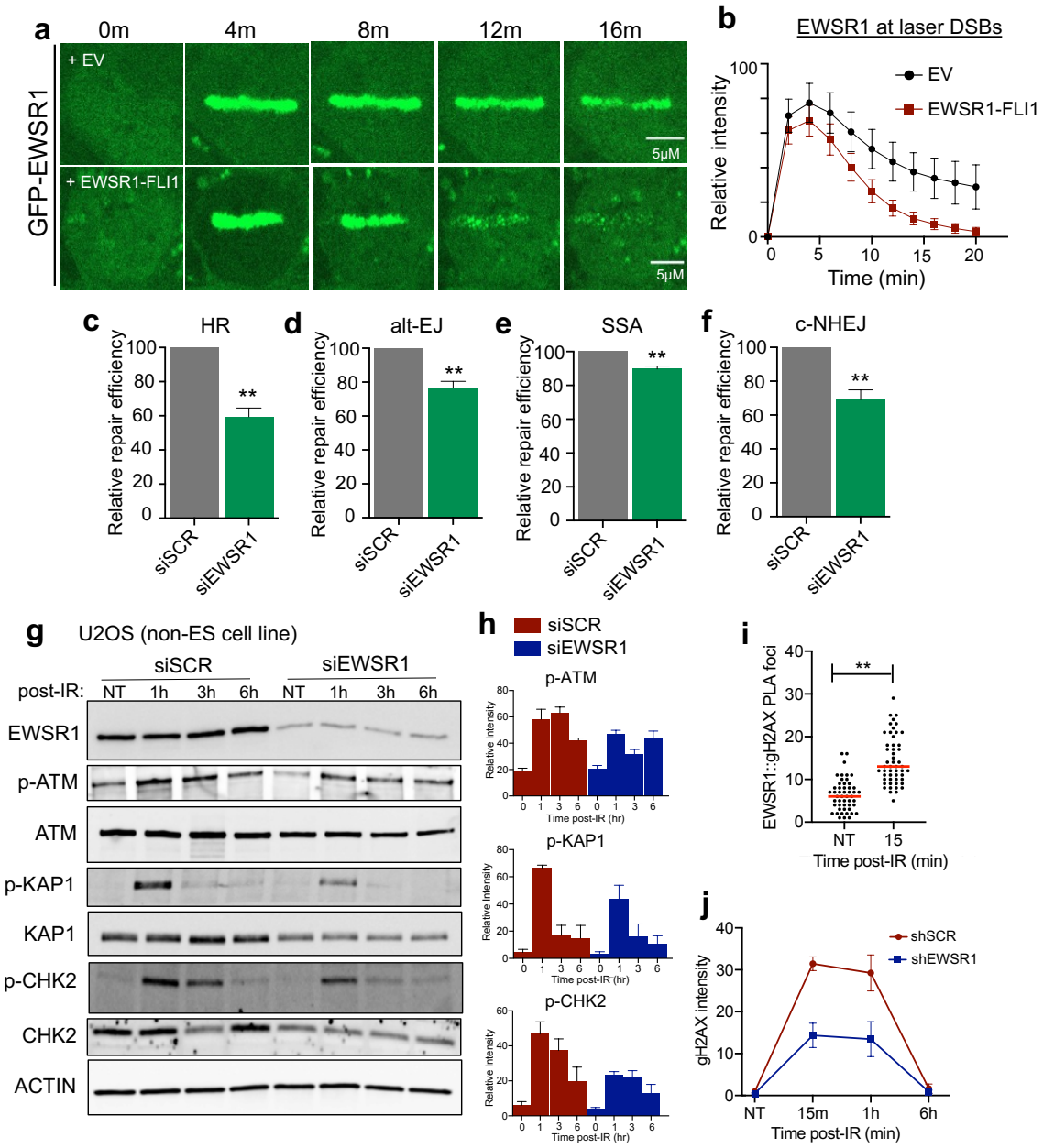

Figure 6: Loss of native EWSR1 phenocopies the DNA repair defects of EWSR1-FLI1.
A, B) Representative images and quantification of laser micro-irradiation in GFP-EWSR1 expressing non-ES cells (U2OS) +/- EWSR1-FLI1 expression. n = 30, 30 cells.
C-F) Relative repair efficiency for pathway-specific DSB repair reporters in U2OS cells. GFP positivity for HR (DR-GFP), alt-EJ (EJ2), SSA, and c-NHEJ (EJ5) upon siRNA knockdown of native EWSR1 or siScramble (siSCR) control assessed at 72 hours.
G, H) Representative Western blot and quantification upon IR (5Gy) at indicated time points in a non-ES cell line (U2OS) after 72 hours siRNA treatment (siEWSR1 or siSCR).
I) Proximity ligation assay (PLA) between native EWSR1 and gH2AX in U2OS cells upon IR (5Gy) at indicated time points.
J) gH2AX intensity measured by flow cytometry after 5 Gy IR in U2OS cells infected with shRNA against native EWSR1 or empty vector (EV) control. $p<0.05$ by paired t-test.
For all panels, error bars represent ± SEM, ** denotes $p < 0.01$ by paired t-test with at least 3 replicates for each panel.

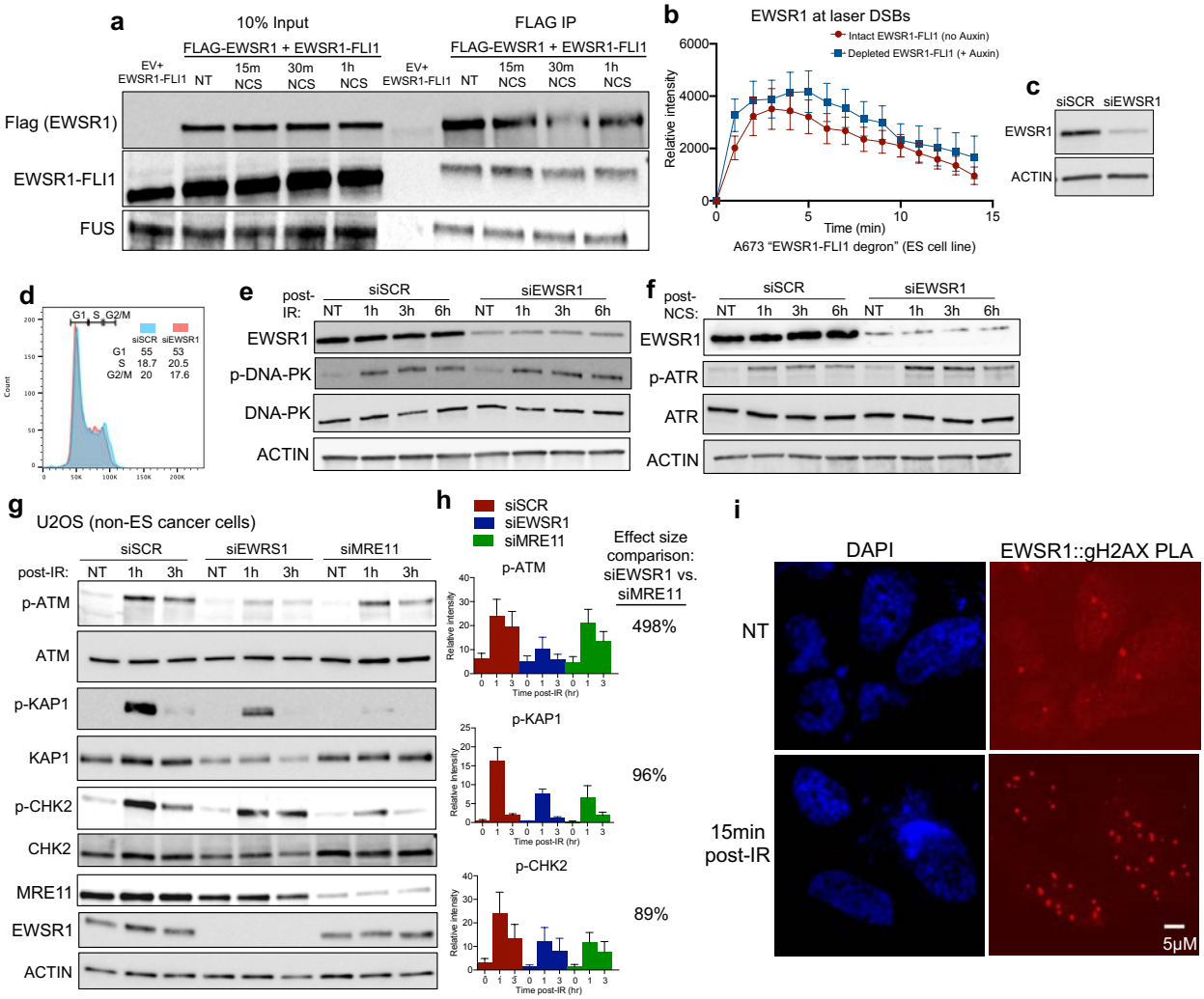

Supplementary Figure 6: Loss of native EWSR1 phenocopies the DNA repair defects caused by EWSR1-FLI1.

A) Immunoprecipitation (IP) of FLAG-tagged EWSR1 expressed in 293T cells +/- EWSR1-FLI1.

B) Laser micro-irradiation of GFP-EWSR1 expressing A673 "EWSR1-FLI1" degron cells +/- 200 μM IAA (auxin). n = 25, 25 cells.

C) Representative Western blot of native EWSR1 knockdown by siRNA in U2OS cells.

D) Cell cycle profiles using Propidium Iodide (PI) in U2OS cells with siRNA against EWSR1 (or Scramble, siSCR).

E, F) Representative Western blots upon 5 Gy IR (E) or 200 ng/ml NCS treatment (F) at indicated time points in a non-ES cell line (U2OS) after 72-hour siRNA treatment against EWSR1 or scramble control.

G, H) Western blotting and quantification after IR (5 Gy) at indicated time points in non-ES U2OS cells with siSCR, siEWSR1, or siMRE11 treatment for 72 hours. Effect size comparison of siEWSR1 to siMRE11 in terms of ATM suppression (p-ATM/p-CHK2/p-KAP1) based on 1hr time point post-IR. % represents ratio of reduction from baseline (siSCR) of siEWSR1 vs. siMRE11.

I) Representative images from Proximity ligation assay (PLA) between native EWSR1 and gH2AX in U2OS cells upon IR at indicated time points.

For all panels, error bars represent ± SEM for at least 3 replicates for each panel.

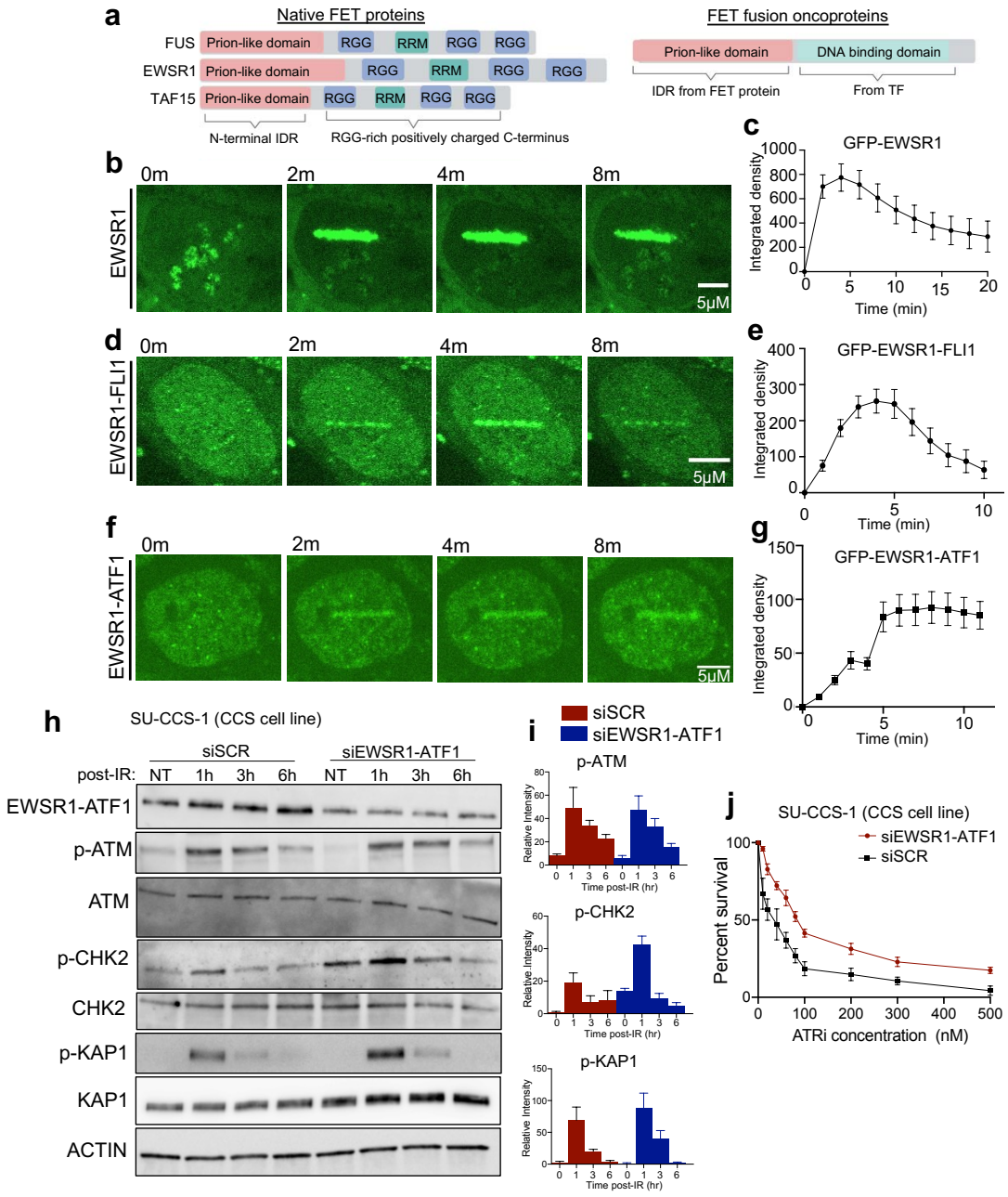

Figure 7: FET fusion oncoproteins are recruited to DNA DSBs.

A) Structure schematic of FET proteins with N-terminal intrinsically disordered regions (IDR) and C-terminal Arginine-glycine-glycine (RGG) repeats, not present in FET fusion oncoproteins like EWSR1-FLI1.

B-G) Representative images and quantification of protein accumulation at laser-induced DSBs in U2OS cells expressing either GFP-EWSR1 (B, C), GFP-EWSR1-FLI1 (D, E), or GFP-EWSR1-ATF1 (F, G). Quantification of at least 30 cells in 3 replicates.

H, I) Western blotting and quantification after IR (5 Gy) in CCS cell line SU-CCS-1 upon 72 hour siRNA treatment against EWSR1-ATF1 or Scramble (siSCR) control.

I) ATR inhibitor (elimusertib) dose-response curves for CCS cell line SU-CCS-1 upon siRNA against EWSR1-ATF1 or siSCR, $p<0.05$ by paired t-test, n=3.

For all panels, error bars represent ± SEM, at least 3 replicates for each panel.

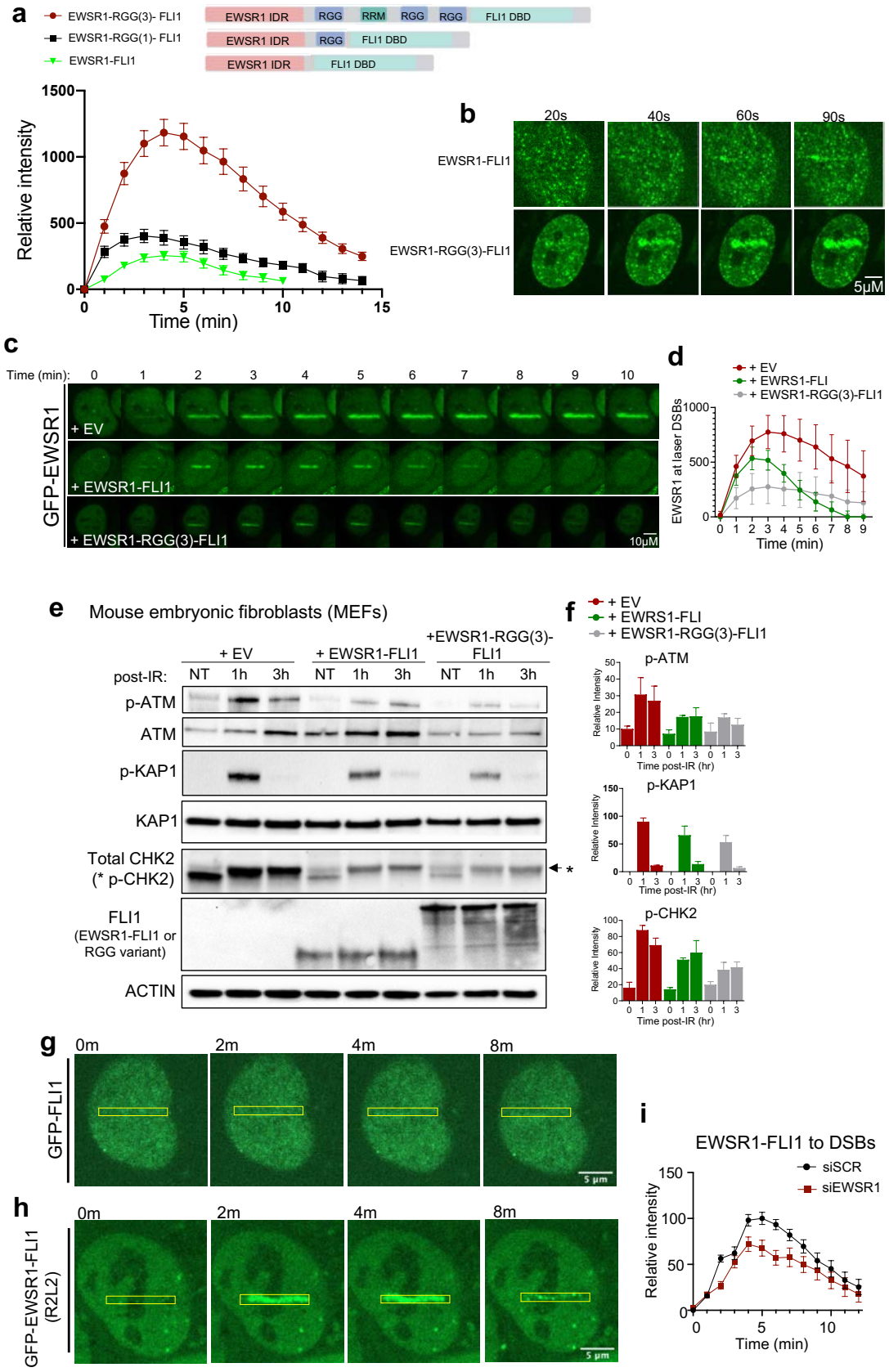

Supplemental Figure 7 continues on next page

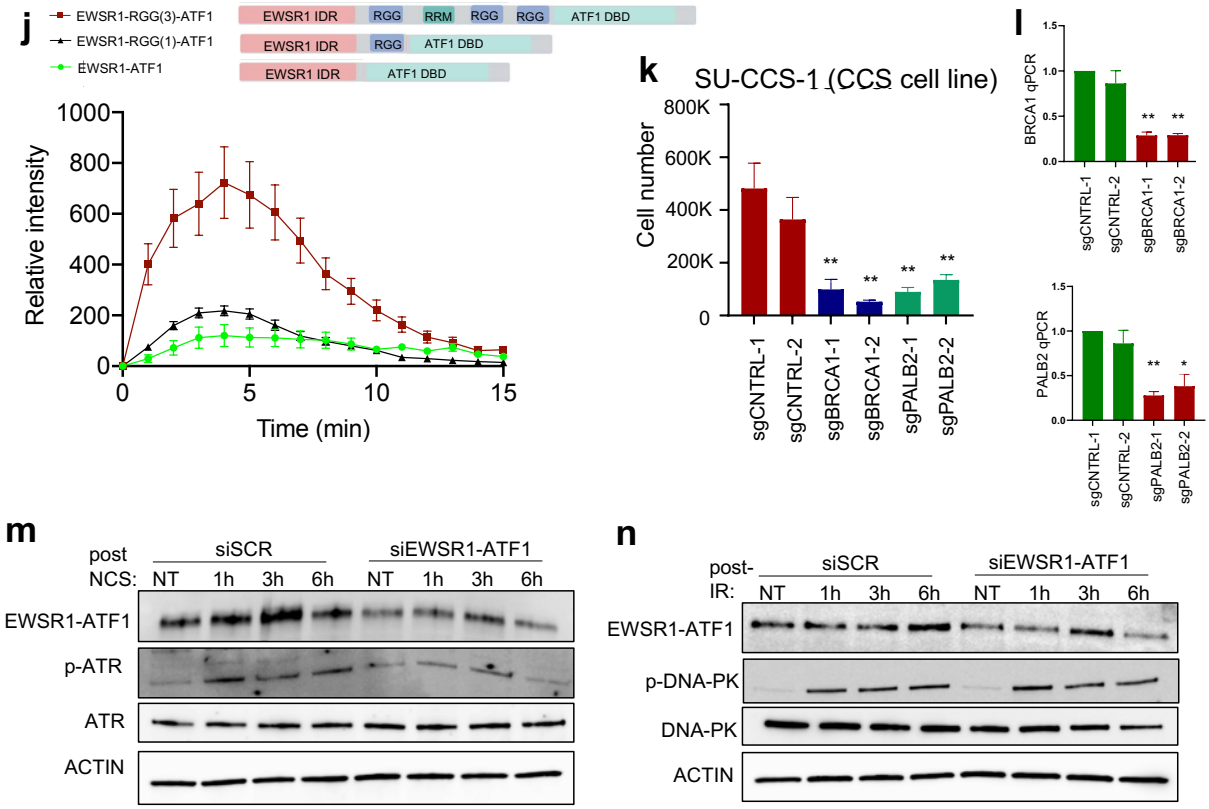

Supplementary Figure 7: FET fusion oncoproteins are recruited to DNA DSBs.

A, B) Structure schematic of RGG containing versions of EWSR1-FLI1. DBD denotes DNA-binding domain. Representative image and quantification of laser-induced DSB accumulation of GFP-tagged constructs in U2OS cells.

C, D) Representative image and quantification of laser-induced DSB accumulation of GFP-EWSR1 in U2OS cells upon expression of empty vector (EV), EWSR1-FLI1, or EWSR1-RGG(3)-FLI1.

E, F) Western blotting and quantification after IR (5 Gy) at indicated time points in MEFs infected with EV, EWSR1-FLI1, or EWSR1-RGG(3)-FLI1.

G, H) Laser micro-irradiation of GFP-tagged full-length FLI1 or DNA binding deficient mutant (R2L2) of EWSR1-FLI1.

I) Quantification of GFP-EWSR1-FLI1 accumulation at laser-induced DSBs in a non-ES cell line (U2OS) upon siRNA against native EWSR1 or scramble (siSCR) for 72 hours. n= 28, 27 cells, $p<0.01$ using paired t-test.

J) Structure schematic of RGG containing versions of EWSR1-ATF1 and quantification of laser-induced DSB accumulation of GFP-tagged constructs in U2OS cells.

K) Growth assays in dCas9 expressing CCS cell line SU-CCS-1 upon introduction of 2 independent sgRNAs against BRCA1, PALB2, or control. n = 4.

L) Relative gene knockdown of each sgRNA by qPCR in SU-CCS-1 cells, n = 3.

M, N) Representative Western blots upon 200 ng/ml NCS treatment (M) or 5 Gy IR (N) in CCS cell line (SU-CCS-1) after 72-hour siRNA treatment against EWSR1-ATF1 or scramble (SCR) control.

For all panels, error bars represent ± SEM, at least 3 replicates for each panel. ** denotes $p < 0.01$, * denotes $p < 0.05$ by paired t-test.

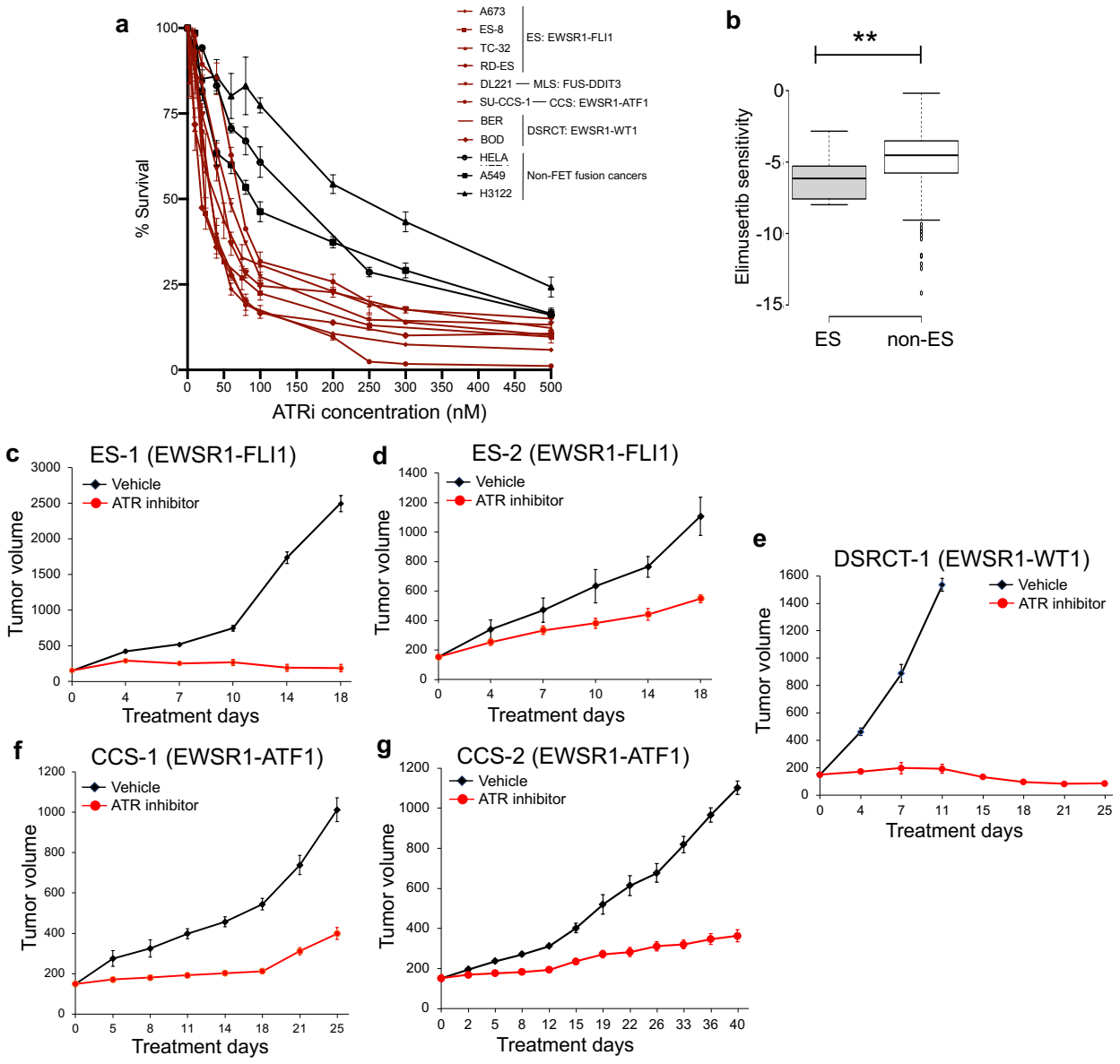

Figure 8: Anti-tumor activity of ATR inhibitor elimusertib in FET fusion PDXs.
A) ATR inhibitor (elimusertib) dose-response curves for FET rearranged (red) and non-FET fusion driven cancer cell lines.
B) Analysis of DepMap Elimusertib sensitivity scores with samples divided into Ewing sarcoma (ES) and non-ES samples. ** denotes $p<0.01$ using unpaired t-test.
C-G) Tumor volume measurements (mm^3) of 5 FET rearranged PDX tumors treated with vehicle or elimusertib 40 mg/kg twice daily per oral gavage, on a 3 days-on/4 days-off schedule. All five models show significant anti-tumor responses with $p<0.01$ by unpaired T-test.
For all panels, error bars represent ± SEM, at least 3 replicates in panel A, 4-8 mice per arm of PDX experiment.

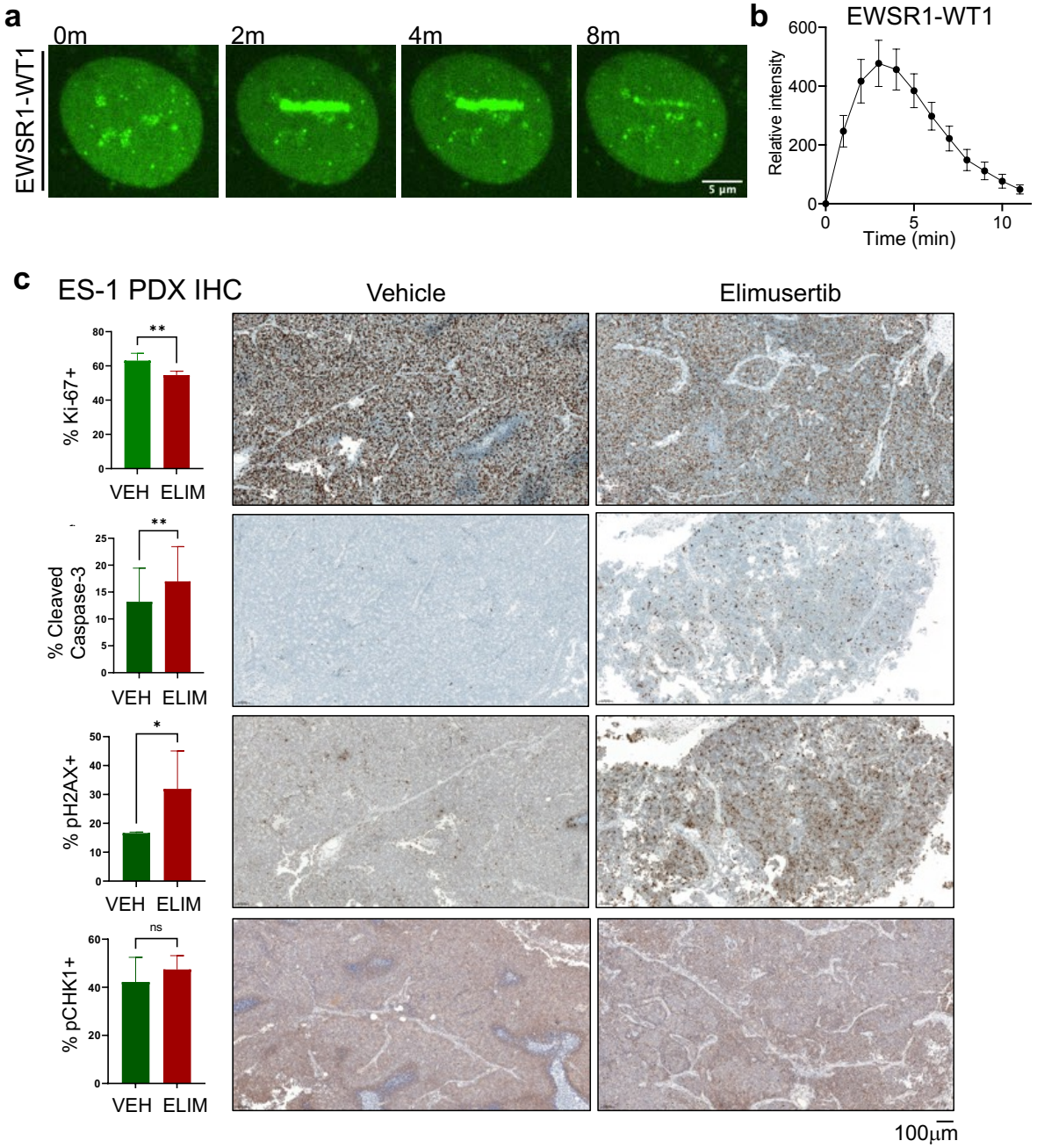

Supplementary Figure 8 continues on next page

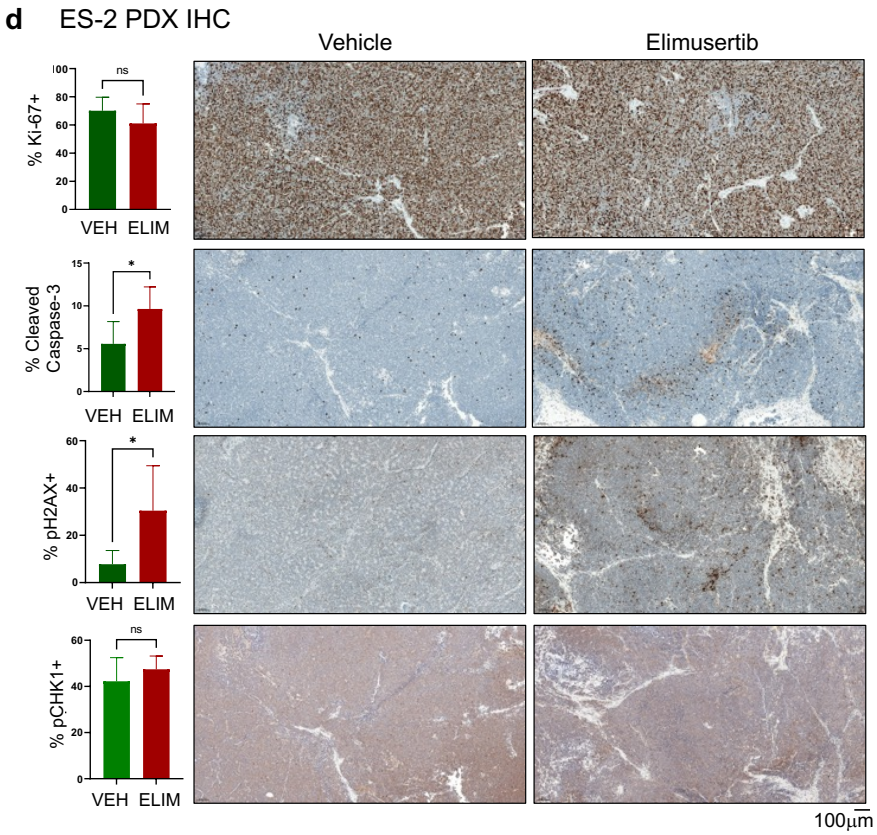

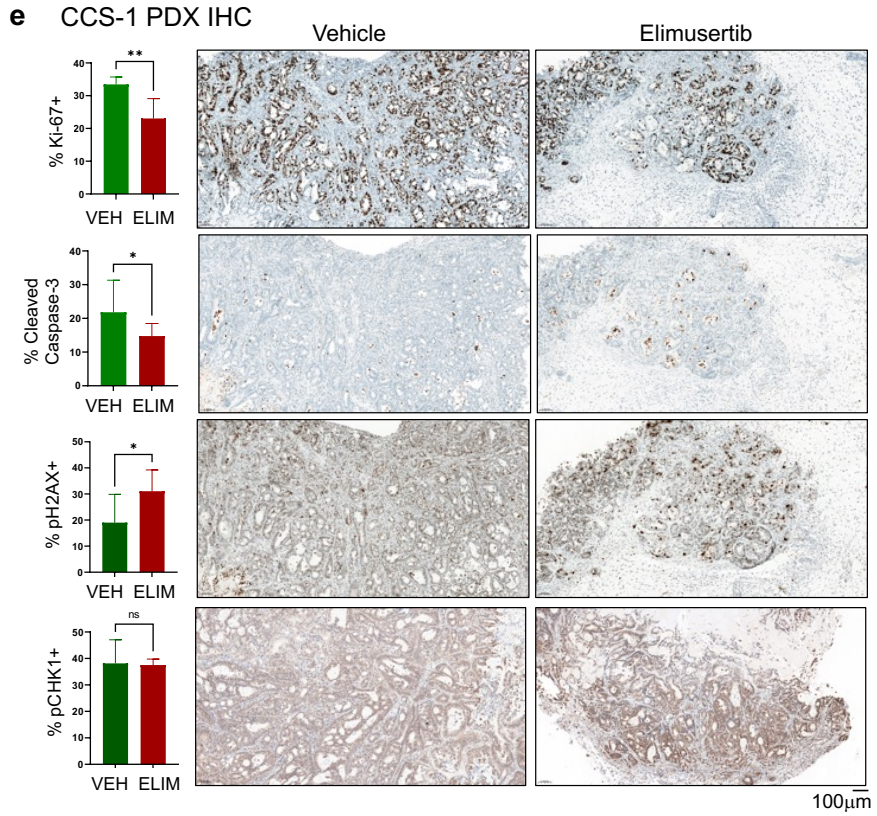

Supplementary Figure 8 continues on next page

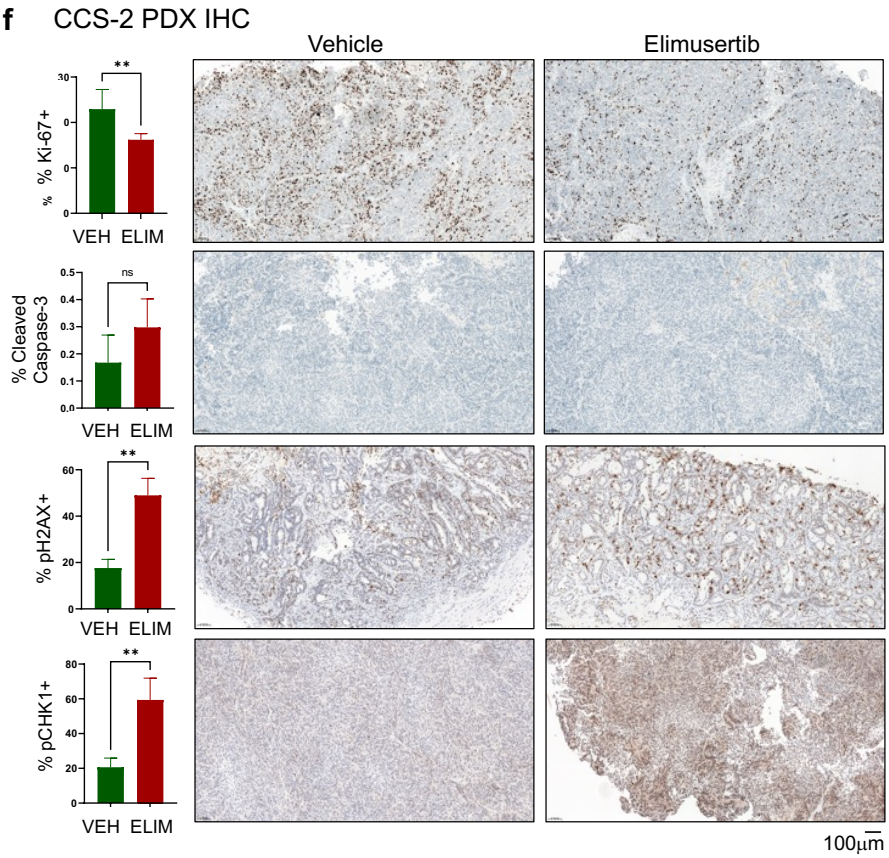

Supplemental Figure 8: Anti-tumor activity of ATR inhibitor elimusertib in FET fusion PDXs.

A, B) Representative images and quantification of protein accumulation at laser-induced DSBs in U2OS cells expressing GFP-EWSR1-WT1. Quantification of at least 30 cells in 3 replicates. C-F) Immunohistochemistry (IHC) staining quantification and representative fields of PDX tumors at end of therapy. VEH refers to vehicle treated tumors; ELIM are elimusertib treated. Automated quantification using QuPath. Note DSRCT PDX experiment still ongoing at time of submission. Error bars represent ± SEM, * denotes $p<0.05$, ** denotes $p<0.01$, unpaired T-test.

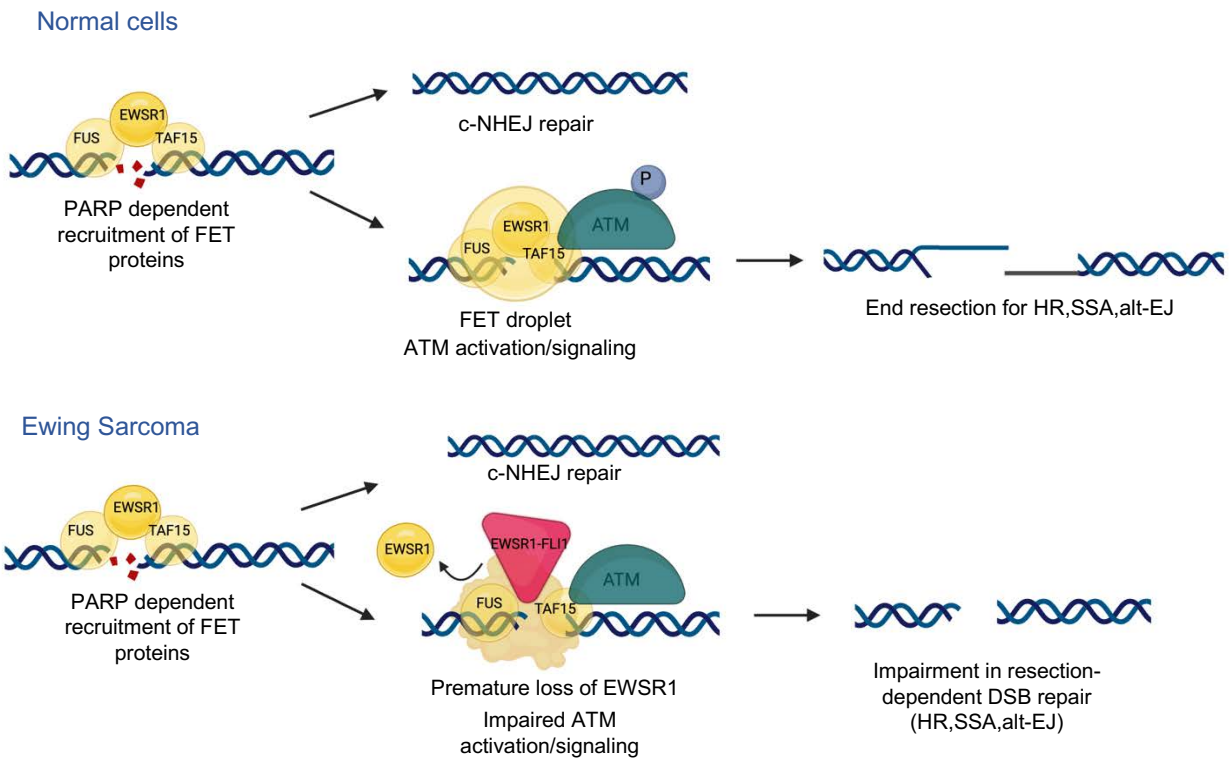

Figure 9: Model of native FET proteins and EWSR1-FLI1 in DSB repair.
Schematic of native FET proteins coordinating early DSB repair responses including rapid c-NHEJ repair and slower ATM activation and resection-dependent DSB repair. In ES, aberrant recruitment of EWSR1-FLI to DSB sites causes premature loss of native EWSR1 resulting in impaired ATM activation/signaling and resection-dependent DSB repair.

Supplementary Note 1:

We compared our CRISPRi screening results with the DepMap project cancer cell line database (https://depmap.org/portal)[78]. Our analysis shows a statistically significant, but modest, difference in the distribution of PALB2 dependence scores when comparing Ewing sarcoma (ES) cell lines with the larger non-ES cancer cell line database, but no significant difference for BRCA1. We hypothesize that these differences may reflect the challenge of studying "essentiality" for double-strand break (DSB) repair genes using a catalytically active Cas9 nuclease that generates DSBs, which was our initial rationale for selecting a CRISPRi-based approach.

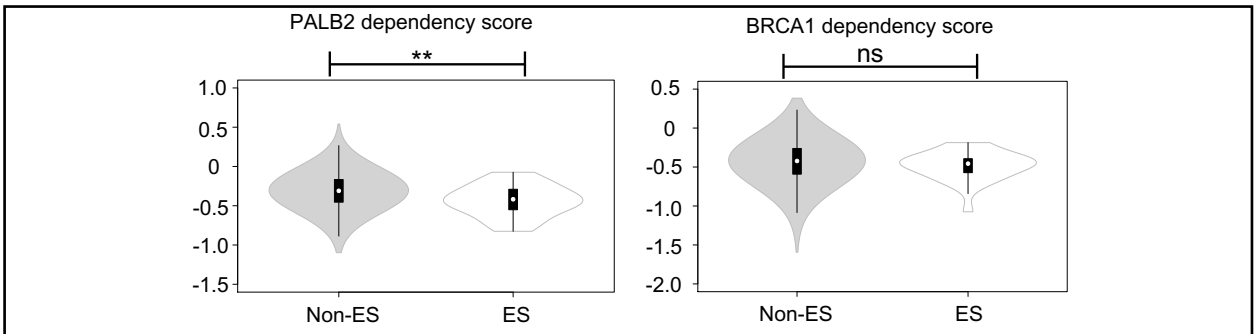

Analysis of DepMap CRISPR score (DepMap Public 24Q2+Score, Chronos) stratified by cell line. ** denotes p<0.01, ns denotes not significant using unpaired t-test. 25 ES cell lines in a total of 1150 cancer cell line database.

In support of this hypothesis, we noted a large discrepancy in the essentiality of these homologous recombination (HR) genes between CRISPR/Cas9 nuclease and RNAi screens in the DepMap database, with a much higher percentage of cancer cell lines found to be dependent on PALB2 and BRCA1 when assayed using a catalytically active Cas9 nuclease.

Gene	% Dependent Cancer Cell Lines in CRISPR/Cas9 screens	% Dependent Cancer Cell Lines in RNAi screens
PALB2	317/1150 = 27.5%	5/550 = 0.9%
BRCA1	509/1150 = 44.2%	16/710 = 2.3%

We also directly compared CRISPRi to RNAi gene knockdown for many of the hits from the screen and found overall more efficient gene knockdown/larger phenotypes using CRISPRi,

similar to the initial publication describing CRISPRi where they made the same comparison (Gilbert et al, 2014[27], Fig. 1E). Consistent with our experience, the more limited set of ES cell lines in the RNAi screening database did not show a statistically significant difference in terms of PALB2 or BRCA1 dependence. Our results highlight important differences between genetic screening modalities (as noted previously by many groups[79,80]) and a potential advantage of CRISPR interference-based approaches for studying DNA repair genes.

Supplementary Note 2:

We note here the significant disparity between the relatively rare occurrence of TP53 (6-10%) mutations in ES patient tumors[34,73], especially at diagnosis, compared to the frequent TP53 mutations seen in ES cell lines. For example, 13 of the 17 annotated ES cell lines in DepMap are TP53 mutant. There is a similar but less dramatic discrepancy between the frequency of both STAG2 mutations (15-20%) and CDKN2A/B loss (12-15%) in patient tumors compared to ES cell lines. We therefore included cell lines with wild-type TP53, STAG2, CDKN2A/B (none are wild-type for all three to our knowledge) to address possible contributions to the observed ATM defects. The TP53, STAG2, and CDKN2A/B status of the major cell lines used in this manuscript are:

1) A673 (TP53 mutant, STAG2 wild-type, CDKN2A/B loss,)[34,72]

2) TC-32 (TP53 wild-type, STAG2 mutant, CDKN2A/B loss)[81,82]

3) TC-252 (TP53 wild-type, STAG2 mutant, CDKN2A/B loss)[82,83].

4) ES-8 (TP53 mutant, STAG2 mutant, CDKN2A intact)[13,82].

Thus, we include data from 2 cell lines with wild-type TP53 (TC-32 and TC-252), 1 cell line with wildtype STAG2 (A673) and 1 cell line with the CDKN2A/B locus intact (ES-8). We also validate

the core findings of ATM suppression and ATR inhibitor sensitivity using an inducible EWSR1-FLI1 shRNA in A673 (STAG2 wild-type) and TC-32 (TP53 wild-type) cells (Fig. 4). Therefore, we conclude that the observed ATM defects do not depend on TP53 (or STAG2, CDKN2A/B) status, though we do not formally test potential roles for these mutations by generating wildtype/mutant isogenic paired cell lines and thus cannot fully exclude possible contributions.

Methods:

Cell lines and culture conditions. U2OS, DL-221, HeLa, and 293T cells were cultured in Dulbecco's Modified Eagle Medium (DMEM)-High glucose (Cytiva) supplemented with 10% fetal calf serum (FCS) and streptomycin/penicillin (100 µg/ml). A673, TC-32, ES-8, RD-ES, SU-CCS-1, A549, H3122, and HCC364 cells were grown in RPMI-1640 (Gibco) supplemented with 10% FCS and streptomycin/penicillin (100 µg/ml). BER and BOD cells were cultured in DMEM/F12-High glucose with 10% FCS. Cell lines were maintained at 37 °Celsius in a humidified incubator with 5% CO2. All cell lines were subjected to STR analysis and mycoplasma testing.

A673 cells with a doxycycline(dox)-inducible shRNA against EWSR1-FLI1 were a kind gift from Franck Tirode[30] (clone 1c); the shRNA sequence (GGCAGCAGAACCCTTCTTAT) targets the EWSR1-FLI1 junction. TC-32 cells with a dox-inducible shRNAs against EWSR1-FLI were a kind gift from Dr. David McFadden and the shRNA sequence (ATCCGACCGAGTCGTCCATGTA) targets the 3' portion of FLI present in the EWSR1-FLI fusion (native FLI1 is not expressed in TC-32 cells). A673 "EWSR1-FLI1 degron" cells were also a kind gift from Dr. David McFadden and the experimental details regarding cell line generation are referenced in McGinnis et al, 2024, bioRxiv[46]. MEF models of ataxia telangiectasia-like disease (ATLD)[47] or Nijmegen breakage syndrome (NBS)[61] were a kind gift from Dr. John Petrini.

CRISPR-interference screen. Ewing sarcoma cell line A673 was transduced with dCas9-KRAB-BFP and then doubly sorted for BFP positive cells. Lentiviral particles were generated from 293T cells transduced with pooled sgRNA libraries (7000 genes, 10 guides per gene) as described previously[27] and then used to infect A673 dCas9-KRAB cells at a multiplicity of infection of 0.3. Cells were selected in puromycin for 48 hours and an aliquot was frozen for t_0 analysis. The remainder of cells were seeded in 500 cm^2 tissue culture plates at equal density (1×10^7 cells/plate) and then treated with vehicle (DMSO) or 12.5 nM/40 nM doxorubicin for 72 hours. After 72 hours, cells were trypsinized, counted and pooled every 3 days, and then replated in media without doxorubicin at the same density to maintain minimum 500× coverage of each sgRNA construct. Cells were viably frozen after 10 days and cell counts were used to determine actual lethal dose (LD) values. 2 biologic replicates were performed, and data combined.

Deep sequencing and data analysis were performed as described[27]. Briefly, genomic DNA was extracted from t_0 and t_{end} cells using a DNEasy Blood & Tissue kit (Qiagen), digested to enrich for lentiviral integration sites, and sgRNA sequences were amplified by PCR for subsequent sequencing on an Illumina HiSeq. Reads were aligned to the sgRNA library and fold-change from t_0 to t_{end} in the DMSO, low and high doxorubicin conditions were calculated. A gene-level score was then calculated as the mean of the top 3 scoring sgRNAs targeting a given transcript.

CRISPRi growth assays. dCas9-KRAB expressing cells were infected with gRNAs (sequences below) and then selected with puromycin for 48 hours. 50,000 cells were then re-plated in a 6 well plate and cell counts were obtained by trypsinization and counting at day 5. For experiments in A673 cells with dox-inducible shRNA against EWSR1-FLI1, 1µg/ml Dox (or vehicle) was added upon replating the puromycin selected, gRNA-expressing cells. gRNA sequences are as follows:

sgBRCA1-1: GCGTAAGGCGTTGTGAACCCT
sgBRCA1-2: GCTCGCTGAGACTTCCTGGAC
sgPALB2-1: GCGCACTGAGGGTGCGATCC

sgPALB2-2: GATTTAATTGGCCGGAGTTT

sgControl-1: GGCTCGGTCCCGCGTCGTCG

sgControl-2: GAACGACTAGTTAGGCGTGTA

Computational analysis of genomic data. Whole genome sequencing (WGS) data from known BRCA mutant/wildtype breast cancer patient samples and Ewing sarcoma samples were obtained from the European Genome-phenome Archive (EGA). The WGS data for the ES cohort was published in Tirode et al, 2014[34] and deposited with study accession numbers: EGAS00001000855 (Institute Curie cohort) and EGAS00001000839 (St. Jude's cohort). The breast cancer WGS was reported in 2016[35] and deposited under EGAD00001001322, as part of a larger WGS of 560 breast cancer samples (overall project accession number EGAS00001001178).

FASTQ files were aligned to the GRCh38 (patch 5) human genome reference using BWA MEM[84], with pre- and post-alignment filtering and processing using NGSUtils[85] and GATK[86]. Insertions and deletions (indel) were called using MuTect 2 for short indels[87] and Delly for larger indels[88]. For each indel, the amount of microhomology at the flanking ends was calculated using the custom software "mhscan". Briefly, for each indel, mhscan will determine the number of bases of homology between the insert or deletion and the flanking sequence. All indels with between 2-6 bp of homology were classified as microhomology (MH) positive. Mutational signatures were calculated using the somatic single-nucleotide variants for each sample. COSMIC v2[89,90] signatures were calculated using deconstructSigs[91].

Determining deletion length bins. The binning ranges were determined by calculating the ability for the number of deletions of each length (1-100 bp) to accurately separate the BRCA wild type (wt) / mutant (mut) samples into two groups. The deletions were classified as either MH-positive or MH-negative and the total number of deletions for each length was calculated for BRCA wt and BRCA mut samples (data were aggregated for all samples in the group). For each deletion length,

a Fisher exact test was used to calculate the statistical significance of whether the MH-positive to MH-negative ratio separated the BRCA wt/mut groups (Fig. S2F). The distribution of p-values was used to determine appropriate bin sizes for downstream analysis. Deletions were binned into ranges of 1-6 bp, 7-28 bp, 29-45 bp, 46-100 bp, and 101-1000 bp.

DSB Repair reporter assays. HR, Alt-EJ, SSA and c-NHEJ efficiencies were measured using previously established DR-GFP, EJ2-GFP, SA-GFP and EJ5-GFP reporter systems respectively[38]. Briefly, dual promoter plasmids co-expressing mTagBFP and EWSR1-FLI1 (or empty vector, EV) were generated by replacing the puromycin cassette with mTagBFP in the plasmid pCDH-CMV-EWSR1-FLI1 (Addgene #102813). Co-expression plasmids were delivered by nucleofection into U2OS DSB reporter cell lines using the SE Cell Line 4D-Nucleofector XL Kit (Lonza Biosciences). To induce a DSB, the I-SceI-P2A-mCherry plasmid which we generated by replacing AmCyan with I-SceI in the bicistronic plasmid Amcyan-P2A-mCherry (Addgene #45350) was delivered by nucleofection after 24 hours. Flow cytometry was performed 72 hours after I-SceI introduction. DSB repair efficiency was calculated by determining the percentage of GFP positive cells within the BFP and mCherry double-positive population (see Fig. S3A). For siRNA experiments, siRNA (5nM) was delivered by transfection using Dharmafect transfection reagent (Dharmacon) 72 hours prior to I-SceI introduction. To directly examine junctional sequences after DSB induction for evidence of cNHEJ or alt-EJ (Fig. S3D), we utilized a distinct I-SceI based DSB repair reporter described here[40]. Briefly, 5μg of the NHEJ reporter was transfected into EWSR1-FLI1 (or EV) expressing U2OS cells, GFP+ cells were sorted at 72 hours for genomic DNA isolation, and then DSB junctional sequences analyzed by recircularization of the repaired NHEJ reporter and plasmid sequencing.

DDR signaling experiments. For experiments in A673 and TC-32 cells with dox-inducible shRNA against EWSR1-FLI1, knockdown was induced by either addition of 1μg/ml dox (A673) or 200 ng/mL (TC-32) for 72 hours followed by IR treatment. For A673 “EWSR1-FLI1 degron” cells,

200 μM IAA (auxin, Sigma) was added 3 hours prior to IR treatment for EWSR1-FLI1 depletion. For the ectopic expression experiments in U2OS cells, the respective fusion proteins (EWSR1-FLI1-GFP, EWSR1-ATF1-GFP, or EV-GFP) were introduced via nucleofection with homemade buffers (Solution 1: 2g ATP-disodium salt, 1.2g $MgCl_2.6H_20$ in 10ml water; Solution 2: 6g KH_2PO_4, 0.6g $NaHCO_3$, 0.2g Glucose in 500ml water, pH 7.4. Solutions were stored at -20°C and 80μl of Solution1 was mixed with 4ml of solution 2 at the time of nucleofection). GFP positive cells were selected by FACS and 24 hours after sorting, subjected to IR. MEF cells were infected with pCDH-EWSR1-FLI1 (Addgene plasmid #102813) lentivirus or EV, selected with puromycin within 72 hours, and then subjected to IR.

For the shRNA experiments testing knockdown of ATM regulators in A673 "EWSR1-FLI1 degron" or MEF cells, Mission pLKO.1 shRNA viruses (sequences below) were used to infect target cells and selection with puromycin was completed within 72 hours to minimize effects on cell viability, followed by IR treatment. For experiments in SU-CCS-1 cells, siRNA against EWSR1-ATF1 was delivered by nucleofection 72 hours prior to IR. For improved induction of ATR/CHK1 signaling, cells were treated with neocarzinostatin (NCS) at 200ng/mL for 30 minutes. Lysates were collected at defined time points post-IR (or post-NCS) and subjected to Western blotting.

Western blotting and quantification. Cells were washed with 1X PBS and scraped in RIPA buffer (25 mM Tris·HCl (pH 7.6), 150 mM NaCl, 1% NP-40, 1% sodium deoxycholate, 0.1% SDS), supplemented with 1X HALT protease inhibitor cocktail and 1X HALT phosphatase inhibitor cocktail. Cells were lysed using a syringe and cellular debris were separated by centrifugation. Lysates were quantified using Bradford's reagent and 15μg lysate was loaded onto SDS-PAGE gels followed by blotting of separated proteins. Blots were blocked with 5% BSA in TBS-T for 30 minutes at room temperature followed by incubation with primary antibody overnight at 4°C. After 1 hour incubation with the appropriate HRP-conjugated secondary antibody, signal was detected using ECL Prime reagent (Amersham, Cytiva) on an ImageQuant LAS 4000. Quantifications were

performed using Fiji and all protein levels were normalized to loading control Actin. To measure CHK2 phosphorylation in MEFs as no reliable mouse p-CHK2 antibody is commercially available, we quantified the intensity of the upper band (after IR) on total CHK2 immunoblots which corresponds to the phosphorylated species, as utilized previously by multiple groups[48,54].

The list of antibodies utilized in this study includes: FLI1 (Abcam, ab133485, 1:500), CtIP (Cell Signaling Technologies (CST), D76F7, 1:000), 53BP1 (Abcam, ab153909, 1:1000), p-ATM (Invitrogen, MA5-32751), ATM (CST, 2873S, 1:1000), pCHK2-T68 (CST, 2661S, 1:1000, Human only), CHK2 (CST, 2662S, 1:1000), p-KAP1 (Novus Biologicals, A700-013, 1:1000), KAP1 (Novus Biologicals, A700-014, 1:1000), p-DNA-PK (CST, 68716S, 1:1000), DNA-PK (CST, 4602T, 1:1000), p-ATR (Genetex, GTX128145, 1:1000), ATR (Novus Biologicals, A300-138A, 1:1000), pCHK1-Ser317: (CST, 2344, 1:1000), CHK1 (CST, 37010, 1:1000), GFP (CST, 2956S, 1:1000), EWSR1 (Genetex, GTX114069, 1:1000), beta-Actin (Sigma, A2228, 1:2000), anti-Flag (Sigma, F3165, 1:2000), ATF1 (Novus Biologicals, A303-036A, 1:1000), FUS (Novus Biologicals, A300-302A-1:1000), RNaseH1 (Genetex, GTX117624, 1:1000), MRE11 (CST, 1:1000, 4895S), NBS1 (CST, 1:1000, 14956), MDC1 (Invitrogen, MA5-27650, 1:1000), RNF8 (Proteintech, 1:1000, 14112-1-AP), RNF168 (EMD Millipore, 1:1000, ABE367, Mouse only), and RNF168 (Thermo, 1:1000, H00165918-MO1, human).

siRNA/shRNA sequences.

siRNA sequences:

EWSR1: Mix of two siRNAs targeting the C-terminus of EWSR1: GGAACAGAUGGGAGGAAGA and AGGAAAGCCCAAAGGCGAU

CTIP: On-TARGETplus SMARTpool siRNA (Dharmacon, L-011376-00-0005)

53BP1: On-TARGETplus SMARTpool siRNA (Dharmacon, L-003548-00-0005)

MRE11: On-TARGETplus SMARTpool siRNA (Dharmacon, L-009271-00-0005)

EWSR1-ATF1: GCGGUGGAAUGGGAAAAAUUU

shRNA targeting sequences (pLKO.1 Mission shRNA):

native EWSR1: TGCATTGACTACCAGATTTAT

LIG4: TATGTCAGTGGACTAATGGAT

Mouse MDC1: mixture of 2 shRNAs, AGCATGCCTCACTCCTATAAG and GAGCCTCAATGGCACTCAAAT

Mouse RNF168: mixture of 2 shRNAs, GCCAACTTCTACTCAAGATAA and CCTTGGCTTCTCCTTTGAGTT

Human MRE11A: mixture of 2 shRNAs, ACGACTGCGAGTGGACTATAG and TGTTGGTTTGCTGCGTATTAA

Human NBS1: mixture of 2 shRNAs, CCTCTTGATGAACCATCTATT, and GCTCGAAAGAATACAGAACTA

Human MDC1: mixture of 2 shRNAs, CCCTGAATCAACTGTCCCTAT, CGGACCAAACTTAACCAAGAA

Human RNF168: mixture of 2 shRNAs, GCAGTCAGTTAATAGAAGAAA, and CGTGGAACTGTGGACGATAAT

Human RNF8: mixture of 2 shRNAs, TGGAGCAACTAGAGAAGACTT, and CCAAAGAATGACCAAATGATA

Cell survival assays. 350,000 cells were seeded in 6-well plates, 24 hours prior to drug treatment. Cells were treated with varying doses of ATR kinase inhibitor elimusertib (Selleckchem) +/- doxorubicin (Sigma) or CHK1 inhibitor LY2603618 (Selleckchem) for 3 days at the end of which cells were counted to determine fractional cell survival. For dox-inducible EWSR1-FLI1 knockdown in A673 and TC-32 cells, shRNA was induced by treatment with dox for 72 hours prior to ATR or CHK1 inhibitor treatment. For RNAseH1 experiments, A673 cells were infected with pLV-EF1a-RNAseH1-IRES-Blast lentivirus (derived from Addgene plasmid #85133) or empty vector and selected for stably infected cells.

gH2AX flow cytometry and immunofluorescence (IF). EWSR1-FLI1 (or EV) expressing U2OS cells were obtained by nucleofection as above. U2OS cells with shRNA against LIG4 or native EWSR1 were obtained through puromycin selection with Mission pLKO.1 shRNA expressing vectors with sequences as above. Cells were treated with 5Gy IR and harvested at 15 minutes

and 1, 3, 6 hours post-IR. After washing with 1ml ice cold PBS, cells were resuspended in 300µl 1X PBS and 700µl of 100% ice-cold ethanol dropwise while gently vortexing the tubes and then incubated overnight at -20°C. The next day, cells were washed with 1x PBS and incubated for 15min at room temperature (RT) in 1.5 mL wash buffer (1% BSA containing 0.25% Triton X-100 in PBS). After centrifugation, cells were incubated in 200 µL of α-phospho H2AX FITC conjugate (JBW301, Millipore, 1:500 in wash buffer) for 2 hours at RT in the dark. Cells were then resuspended in 300-500 µl PI solution for 60 min at RT in the dark prior to flow cytometry analysis. For IF studies in A673 "EWSR1-FLI1 degron" cells, 200 µM IAA (auxin, Sigma) was added 3 hours prior to IR. IF performed using standard protocols with fixation for 15 minutes in 4% formaldehyde, primary antibodies, gH2AX (CST, 9718, 1:400) or p-ATM (Rockland, 200-301-400, 1:200) incubated overnight at 4 degrees.

Laser micro-irradiation. Laser micro-irradiation was performed as previously described[21]. Briefly, U2OS cells expressing EWSR1-GFP, EWSR1-FLI1-GFP, EWSR1-ATF1-GFP, or the various mutant forms of the fusion oncoproteins were seeded in 8-well Lab Tek II Chamber Slides (Thermo Fisher Scientific) for 24 hours. Cells were treated with 1µg/ml Hoechst 33342 (Thermo Fisher Scientific) for 30 minutes prior to micro-irradiation. Live cell microscopy was performed using Nikon Ti microscope with a CSU-W1 spinning disk confocal using a 100X/1.4 Plan Apo VC objective at the UCSF Center for Light Microscopy. To induce DNA damage, 5 pixel wide stripes were drawn in every cell nucleus to label the region of interest (ROI) and irradiated with a 405nm diode laser (40mW). The experiments in EWSR1-GFP expressing U2OS cells comparing the effects of EWSR1-FLI1, EWSR1-RGG(3)-FLI1, and EV were performed at MSKCC. Plasmids were delivered by nucleofection, then sensitized with BrdU (5 µM) for 24 hours. Laser micro-irradiation was performed using the 405 bleaching laser at 100% power using a Leica-SP8 confocal microscope with an ROI (0.1 x 11 µm), which yielded comparable recruitment kinetics to the experiments at UCSF. In both cases, images were acquired pre-irradiation and at 1 minute

intervals post-laser damage for 15 minutes. To plot recruitment kinetics, the pre-irradiation fluorescence intensity was subtracted from the intensity of the ROI for every nucleus.

Proximity ligation assay. U2OS cells were seeded on autoclaved coverslips and subjected to 10Gy IR. 15 minutes post-IR, cells were washed twice with 1X PBS and fixed with 4% formaldehyde for 15 minutes at room temperature. Fixed cells were incubated with 0.5% Triton X-100 for 10 minutes. Cells were then washed twice with 1X PBS and blocked in 5% BSA/1X PBS solution for 1 hour at room temperature. Coverslips were then incubated overnight at 4 °C with EWSR1 (Origene, 1:200) and gH2AX (CST, 1:500) antibodies. The following day proximity ligation assay (PLA) was performed using Duolink PLA technology (Sigma-Aldrich) according to the manufacturer's instructions. Images were acquired using Nikon Ti microscope with a CSU-W1 spinning disk confocal using a 100X/1.4 Plan Apo VC objective (Center for Advanced Light Microscopy, UCSF).

EWSR1 Co-Immunoprecipitation (co-IP). 293T cells were transfected with Flag-EWSR1 and EWSR1-FLI1 (or empty vector) for 48 hours. Cells were then treated with NCS (200ng/mL) for 30 minutes and cells were collected at 15 minutes, 30 minutes and 1 hour post NCS treatment. Nuclear co-IP was performed using the Nuclear Co-IP kit (Active Motif) according to the manufacturer's instructions.

Cell cycle analysis. U2OS cells were nucleofected with the dual promoter pCDH-EWSR1-FLI1-EF1a-mtagBFP (or empty vector) and analyzed at 48 hours. Cells were fixed using 4% formaldehyde for 15 minutes at room temperature. After washing with 1% BSA in PBS, cells were resuspended in 500µl of FxCycle™ PI/RNAse Solution (ThermoFisher Scientific) for 30 minutes at room temperature. Cell cycle profiles were also analyzed using Click-iT EdU Alexa Fluor 488 Flow Cytometry Assay Kit (Invitrogen). Cells were pulse labelled with 10µM EdU for 30 minutes and processed according to the manufacturer's instructions. Flow cytometry was used to analyze the cell cycle profile for BFP positive, EWSR1-FLI1 (or empty vector) expressing cells.

Patient-derived xenograft (PDX) experiments. The establishment of PDX models was performed by the laboratory of Dr. Filemon Dela Cruz and Dr. Andrew Kung from patients at MSKCC according to the institutional animal and IRB protocols. Tumor fragments from patients were serially transplanted into athymic nude (Foxn1^{nu}) mice from Charles River Laboratories to establish the PDX for 3-5 passages, after which time seeds were implanted to begin the PDX experiments. When average tumor volumes exceeded 150mm^3, mice were randomized into either elimusertib or vehicle group. Elimusertib was dosed at 40 mg/kg twice daily, 3 days-on/4 days-off as previously reported[75], and dissolved in 60% polyethylene glycol 400, 10% ethanol, and 30% water to a 4 mg/mL solution. The same solution without compound was used as vehicle control. Mice were sacrificed by cervical dislocation once the tumor volume exceeded 2000 mm^3 or body weight loss was higher than 20% (which did not occur), and tumors were collected for immunohistochemistry (IHC).

For IHC studies**,** paraffin cross-sections (thickness = 5μm) of PDX tumor tissues were applied to Superfrost Plus microscope slides (Fisher, #1255015) for immunohistochemical analyses. After heat-mediated antigen retrieval (48 minutes, Cell Conditioning 1) (Ventana, #950-500), PDX tumor cross-sections were incubated for 4 hours at room temperature with the following primary antibodies: rabbit polyclonal Cleaved Caspase-3 (Cell Signaling Technology, #9661, 0.05mg/mL), rabbit monoclonal Ki67 (Cell Signaling Technology, #9027, 0.25mg/mL), gH2AX Ser139 (Cell Signaling Technology, #9718, 1:1,000 dilution), p-CHK1 (Cell Signaling Technology, #2348, 1:100 dilution), or normal rabbit polyclonal control IgG (Invitrogen, #10500C). After sequential washes with PBS, sections were incubated for 20 minutes with Omni Map anti-Rb HRP (Roche, #760-4311), followed by DAB ChromoMap Kit amplification (Ventana Medical Systems, #760-159). The slides were counter-stained with hematoxylin and mounted with Permount (Fisher Scientific). Analysis was performed in a blinded fashion using QuPath software.

Statistics. Data from at least three independent experiments were used to calculate P values which were determined with Student's t tests and ANOVA using GraphPad software.

Data and Code Availability. All data supporting the findings of this study are available within the paper and its Supplementary Information. Code for "mhscan" is available on request.

Author Contributions

SM, DG, TGB, ASC, and AT conceived and designed the study. SM, DG, YPL, AFG, HA, SP, NW, AH, and AT conducted the experiments and collected data. MB designed the computational algorithms and analyzed data. FDC, TF, and EDS performed the PDX experiments. SM, DG, MH, TGB, and AT analyzed and interpreted the data. JW and ASC provided support for the CRISPR screening and computational analysis respectively. SM, TGB, and AT wrote the manuscript.

Acknowledgements

This project is supported by the Tow Center for Developmental Oncology, the V Foundation, Hyundai Hope on Wheels, the Sarcoma Center at MSKCC, NIH/NCI Cancer Center Support Grant P30 CA008748, Alex's Lemonade Stand, the A.P. Giannini Foundation, and the St. Baldrick's Foundation (to A.T), as well as NIH/NCI U54CA224081, R01CA169338, R01CA211052, R01CA204302, U01CA217882 (to T.G.B). A.T. was an advisor to Faze Medicines. T.G.B. is an advisor to Novartis, Astrazeneca, Revolution Medicines, Array/Pfizer, Springworks, Strategia, Relay, Jazz, Rain, EcoR1 and receives research funding from Novartis and Revolution Medicines and Strategia. The authors would like to acknowledge A. Yasemin Goksenin and Zoji Bomya for experimental help, Amit Sabnis, Alan Ashworth, John Petrini, and Alex Kentsis for scientific input and manuscript review, Jeremy Stark for the DNA double-strand

break reporter cell lines, Biorender.com for generation of Fig. 9, and the Center for Advanced Light Microscopy at UCSF for technical help. We especially thank the lab of Dr. David McFadden for sharing unpublished reagents including the A673 “EWSR1-FLI1 degron” cells and TC-32 cells with dox-inducible shRNAs against EWSR1-FLI, as detailed in the Methods.

References:

1 Lanz, M. C., Dibitetto, D. & Smolka, M. B. DNA damage kinase signaling: checkpoint and repair at 30 years. *Embo j* **38**, e101801 (2019). https://doi.org:10.15252/embj.2019101801

2 Di Micco, R. *et al.* Oncogene-induced senescence is a DNA damage response triggered by DNA hyper-replication. *Nature* **444**, 638-642 (2006). https://doi.org:10.1038/nature05327

3 Kotsantis, P., Petermann, E. & Boulton, S. J. Mechanisms of Oncogene-Induced Replication Stress: Jigsaw Falling into Place. *Cancer Discov* **8**, 537-555 (2018). https://doi.org:10.1158/2159-8290.Cd-17-1461

4 Halazonetis, T. D., Gorgoulis, V. G. & Bartek, J. An oncogene-induced DNA damage model for cancer development. *Science* **319**, 1352-1355 (2008). https://doi.org:10.1126/science.1140735

5 Bartkova, J. *et al.* DNA damage response as a candidate anti-cancer barrier in early human tumorigenesis. *Nature* **434**, 864-870 (2005). https://doi.org:10.1038/nature03482

6 Bryant, H. E. *et al.* Specific killing of BRCA2-deficient tumours with inhibitors of poly(ADP-ribose) polymerase. *Nature* **434**, 913-917 (2005). https://doi.org:10.1038/nature03443

7 Farmer, H. *et al.* Targeting the DNA repair defect in BRCA mutant cells as a therapeutic strategy. *Nature* **434**, 917-921 (2005). https://doi.org:10.1038/nature03445

8 *Targeting the DNA damage response for cancer therapy*. 1 edn, (Springer International Publishing, 2023).

9 Schwartz, J., Cech, T. & Parker, R. Biochemical Properties and Biological Functions of FET Proteins. *Annual review of biochemistry* **84** (2014). https://doi.org:10.1146/annurev-biochem-060614-034325

10 Grünewald, T. G. P. *et al.* Ewing sarcoma. *Nature Reviews Disease Primers* **4**, 5 (2018). https://doi.org:10.1038/s41572-018-0003-x

11 Krikelis, D. & Judson, I. Role of chemotherapy in the management of soft tissue sarcomas. *Expert Rev Anticancer Ther* **10**, 249-260 (2010). https://doi.org:10.1586/era.09.176

12 Garnett, M. J. *et al.* Systematic identification of genomic markers of drug sensitivity in cancer cells. *Nature* **483**, 570-575 (2012). https://doi.org:10.1038/nature11005

13 Stewart, E. *et al.* Targeting the DNA repair pathway in Ewing sarcoma. *Cell Rep* **9**, 829-841 (2014). https://doi.org:10.1016/j.celrep.2014.09.028

14 Ewing, J. R. Diffuse endothelioma of bone. . *Proceedings of the New York Pathological Society* **450**, 12:17 (1921).

15 Gorthi, A. *et al.* EWS-FLI1 increases transcription to cause R-loops and block BRCA1 repair in Ewing sarcoma. *Nature* **555**, 387-391 (2018). https://doi.org:10.1038/nature25748

16 Choy, E. *et al.* Phase II study of olaparib in patients with refractory Ewing sarcoma following failure of standard chemotherapy. *BMC Cancer* **14**, 813 (2014). https://doi.org:10.1186/1471-2407-14-813

17 Kondrashova, O. *et al.* Methylation of all BRCA1 copies predicts response to the PARP inhibitor rucaparib in ovarian carcinoma. *Nat Commun* **9**, 3970 (2018). https://doi.org:10.1038/s41467-018-05564-z

18 Lee, J. m., Ledermann, J. A. & Kohn, E. C. PARP Inhibitors for BRCA1/2 mutation-associated and BRCA-like malignancies. *Annals of Oncology* **25**, 32-40 (2014). https://doi.org:10.1093/annonc/mdt384

19 Schwartz, J. C., Cech, T. R. & Parker, R. R. Biochemical Properties and Biological Functions of FET Proteins. *Annual Review of Biochemistry* **84**, 355-379 (2015). https://doi.org:10.1146/annurev-biochem-060614-034325

20 Altmeyer, M. *et al.* Liquid demixing of intrinsically disordered proteins is seeded by poly(ADP-ribose). *Nature Communications* **6**, 8088 (2015). https://doi.org:10.1038/ncomms9088

21 Izhar, L. *et al.* A Systematic Analysis of Factors Localized to Damaged Chromatin Reveals PARP-Dependent Recruitment of Transcription Factors. *Cell Rep* **11**, 1486-1500 (2015). https://doi.org:10.1016/j.celrep.2015.04.053

22 Levone, B. R. *et al.* FUS-dependent liquid-liquid phase separation is important for DNA repair initiation. *J Cell Biol* **220** (2021). https://doi.org:10.1083/jcb.202008030

23 Singatulina, A. S. *et al.* PARP-1 Activation Directs FUS to DNA Damage Sites to Form PARG-Reversible Compartments Enriched in Damaged DNA. *Cell Rep* **27**, 1809-1821.e1805 (2019). https://doi.org:10.1016/j.celrep.2019.04.031

24 Chappidi, N. *et al.* PARP1-DNA co-condensation drives DNA repair site assembly to prevent disjunction of broken DNA ends. *Cell* **187**, 945-961.e918 (2024). https://doi.org:10.1016/j.cell.2024.01.015

25 Kovar, H. Dr. Jekyll and Mr. Hyde: The Two Faces of the FUS/EWS/TAF15 Protein Family. *Sarcoma* **2011**, 837474 (2011). https://doi.org:10.1155/2011/837474

26 Cote, G. M. & Choy, E. Update in treatment and targets in Ewing sarcoma. *Hematol Oncol Clin North Am* **27**, 1007-1019 (2013). https://doi.org:10.1016/j.hoc.2013.07.001

27 Gilbert, L. A. *et al.* Genome-Scale CRISPR-Mediated Control of Gene Repression and Activation. *Cell* **159**, 647-661 (2014). https://doi.org:10.1016/j.cell.2014.09.029

28 Daggubati, V. *et al.* Smoothened-activating lipids drive resistance to CDK4/6 inhibition in Hedgehog-associated medulloblastoma cells and preclinical models. *The Journal of Clinical Investigation* **131** (2021). https://doi.org:10.1172/JCI141171

29 Rosenbluh, J. *et al.* Complementary information derived from CRISPR Cas9 mediated gene deletion and suppression. *Nat Commun* **8**, 15403 (2017). https://doi.org:10.1038/ncomms15403

30 Tirode, F. *et al.* Mesenchymal Stem Cell Features of Ewing Tumors. *Cancer Cell* **11**, 421-429 (2007). https://doi.org:https://doi.org/10.1016/j.ccr.2007.02.027

31 Du, R., Huang, C., Liu, K., Li, X. & Dong, Z. Targeting AURKA in Cancer: molecular mechanisms and opportunities for Cancer therapy. *Molecular Cancer* **20**, 15 (2021). https://doi.org:10.1186/s12943-020-01305-3

32 Coleman, N., Zhang, B., Byers, L. A. & Yap, T. A. The role of Schlafen 11 (SLFN11) as a predictive biomarker for targeting the DNA damage response. *British Journal of Cancer* **124**, 857-859 (2021). https://doi.org:10.1038/s41416-020-01202-y

33 Tang, S. W. *et al.* SLFN11 Is a Transcriptional Target of EWS-FLI1 and a Determinant of Drug Response in Ewing Sarcoma. *Clin Cancer Res* **21**, 4184-4193 (2015). https://doi.org:10.1158/1078-0432.Ccr-14-2112

34 Tirode, F. *et al.* Genomic landscape of Ewing sarcoma defines an aggressive subtype with co-association of STAG2 and TP53 mutations. *Cancer Discov* **4**, 1342-1353 (2014). https://doi.org:10.1158/2159-8290.Cd-14-0622

35 Nik-Zainal, S. *et al.* Landscape of somatic mutations in 560 breast cancer whole-genome sequences. *Nature* **534**, 47-54 (2016). https://doi.org:10.1038/nature17676

36 Polak, P. *et al.* A mutational signature reveals alterations underlying deficient homologous recombination repair in breast cancer. *Nat Genet* **49**, 1476-1486 (2017). https://doi.org:10.1038/ng.3934

37 Nik-Zainal, S. *et al.* Mutational processes molding the genomes of 21 breast cancers. *Cell* **149**, 979-993 (2012). https://doi.org:10.1016/j.cell.2012.04.024

38 Gunn, A. & Stark, J. M. I-SceI-based assays to examine distinct repair outcomes of mammalian chromosomal double strand breaks. *Methods Mol Biol* **920**, 379-391 (2012). https://doi.org:10.1007/978-1-61779-998-3_27

39 Bennardo, N., Cheng, A., Huang, N. & Stark, J. M. Alternative-NHEJ is a mechanistically distinct pathway of mammalian chromosome break repair. *PLoS Genet* **4**, e1000110 (2008). https://doi.org:10.1371/journal.pgen.1000110

40 Seluanov, A., Mao, Z. & Gorbunova, V. Analysis of DNA double-strand break (DSB) repair in mammalian cells. *J Vis Exp* (2010). https://doi.org:10.3791/2002

41 Riggi, N. *et al.* EWS-FLI1 utilizes divergent chromatin remodeling mechanisms to directly activate or repress enhancer elements in Ewing sarcoma. *Cancer Cell* **26**, 668-681 (2014). https://doi.org:10.1016/j.ccell.2014.10.004

42 Nusinow, D. P. *et al.* Quantitative Proteomics of the Cancer Cell Line Encyclopedia. *Cell* **180**, 387-402.e316 (2020). https://doi.org:10.1016/j.cell.2019.12.023

43 Blackford, A. N. & Jackson, S. P. ATM, ATR, and DNA-PK: The Trinity at the Heart of the DNA Damage Response. *Mol Cell* **66**, 801-817 (2017). https://doi.org:10.1016/j.molcel.2017.05.015

44 Chen, C. C. *et al.* ATM loss leads to synthetic lethality in BRCA1 BRCT mutant mice associated with exacerbated defects in homology-directed repair. *Proc Natl Acad Sci U S A* **114**, 7665-7670 (2017). https://doi.org:10.1073/pnas.1706392114

45 Cai, M. Y. *et al.* Cooperation of the ATM and Fanconi Anemia/BRCA Pathways in Double-Strand Break End Resection. *Cell Rep* **30**, 2402-2415.e2405 (2020). https://doi.org:10.1016/j.celrep.2020.01.052

46 McGinnis, J. H. *et al.* Endogenous EWSR1-FLI1 degron alleles enable control of fusion oncoprotein expression in tumor cell lines and xenografts. *bioRxiv*, 2024.2010.2027.620498 (2024). https://doi.org:10.1101/2024.10.27.620498

47 Theunissen, J.-W. F. *et al.* Checkpoint Failure and Chromosomal Instability without Lymphomagenesis in Mre11ATLD1/ATLD1 Mice. *Molecular Cell* **12**, 1511-1523 (2003). https://doi.org:https://doi.org/10.1016/S1097-2765(03)00455-6

48 Kim, J. H. *et al.* The Mre11-Nbs1 Interface Is Essential for Viability and Tumor Suppression. *Cell Reports* **18**, 496-507 (2017). https://doi.org:10.1016/j.celrep.2016.12.035

49 Min, A. *et al.* AZD6738, A Novel Oral Inhibitor of ATR, Induces Synthetic Lethality with ATM Deficiency in Gastric Cancer Cells. *Mol Cancer Ther* **16**, 566-577 (2017). https://doi.org:10.1158/1535-7163.Mct-16-0378

50 Menezes, D. L. *et al.* A synthetic lethal screen reveals enhanced sensitivity to ATR inhibitor treatment in mantle cell lymphoma with ATM loss-of-function. *Mol Cancer Res* **13**, 120-129 (2015). https://doi.org:10.1158/1541-7786.Mcr-14-0240

51 Wengner, A. M. *et al.* The Novel ATR Inhibitor BAY 1895344 Is Efficacious as Monotherapy and Combined with DNA Damage-Inducing or Repair-Compromising Therapies in Preclinical Cancer Models. *Mol Cancer Ther* **19**, 26-38 (2020). https://doi.org:10.1158/1535-7163.Mct-19-0019

52 Uziel, T. *et al.* Requirement of the MRN complex for ATM activation by DNA damage. *The EMBO Journal* **22**, 5612-5621 (2003). https://doi.org:https://doi.org/10.1093/emboj/cdg541

53 Carson, C. T. *et al.* The Mre11 complex is required for ATM activation and the G₂/M checkpoint. *The EMBO Journal* **22**, 6610-6620 (2003). https://doi.org:https://doi.org/10.1093/emboj/cdg630

54 Lou, Z. *et al.* MDC1 maintains genomic stability by participating in the amplification of ATM-dependent DNA damage signals. *Mol Cell* **21**, 187-200 (2006). https://doi.org:10.1016/j.molcel.2005.11.025

55 Chapman, J. R. & Jackson, S. P. Phospho-dependent interactions between NBS1 and MDC1 mediate chromatin retention of the MRN complex at sites of DNA damage. *EMBO reports* **9**, 795-801-801 (2008). https://doi.org:https://doi.org/10.1038/embor.2008.103

56 Wu, J. *et al.* Chfr and RNF8 synergistically regulate ATM activation. *Nature Structural & Molecular Biology* **18**, 761-768 (2011). https://doi.org:10.1038/nsmb.2078

57 Kolas, N. K. *et al.* Orchestration of the DNA-Damage Response by the RNF8 Ubiquitin Ligase. *Science* **318**, 1637-1640 (2007). https://doi.org:doi:10.1126/science.1150034

58 Mailand, N. *et al.* RNF8 Ubiquitylates Histones at DNA Double-Strand Breaks and Promotes Assembly of Repair Proteins. *Cell* **131**, 887-900 (2007). https://doi.org:https://doi.org/10.1016/j.cell.2007.09.040

59 Stewart, G. S. *et al.* The RIDDLE Syndrome Protein Mediates a Ubiquitin-Dependent Signaling Cascade at Sites of DNA Damage. *Cell* **136**, 420-434 (2009). https://doi.org:https://doi.org/10.1016/j.cell.2008.12.042

60 Doil, C. *et al.* RNF168 Binds and Amplifies Ubiquitin Conjugates on Damaged Chromosomes to Allow Accumulation of Repair Proteins. *Cell* **136**, 435-446 (2009). https://doi.org:https://doi.org/10.1016/j.cell.2008.12.041

61 Williams, B. R. *et al.* A Murine Model of Nijmegen Breakage Syndrome. *Current Biology* **12**, 648-653 (2002). https://doi.org:https://doi.org/10.1016/S0960-9822(02)00763-7

62 Lou, Z., Minter-Dykhouse, K., Wu, X. & Chen, J. MDC1 is coupled to activated CHK2 in mammalian DNA damage response pathways. *Nature* **421**, 957-961 (2003). https://doi.org:10.1038/nature01447

63 Soutoglou, E. & Misteli, T. Activation of the Cellular DNA Damage Response in the Absence of DNA Lesions. *Science* **320**, 1507-1510 (2008). https://doi.org:doi:10.1126/science.1159051

64 Boulay, G. *et al.* Cancer-Specific Retargeting of BAF Complexes by a Prion-like Domain. *Cell* **171**, 163-178.e119 (2017). https://doi.org:10.1016/j.cell.2017.07.036

65 Bailly, R. A. *et al.* DNA-binding and transcriptional activation properties of the EWS-FLI-1 fusion protein resulting from the t(11;22) translocation in Ewing sarcoma. *Molecular and Cellular Biology* **14**, 3230-3241 (1994). https://doi.org:doi:10.1128/mcb.14.5.3230-3241.1994

66 Ngoi, N. Y. L. *et al.* Targeting ATR in patients with cancer. *Nature Reviews Clinical Oncology* **21**, 278-293 (2024). https://doi.org:10.1038/s41571-024-00863-5

67 Wengner, A. M. *et al.* The Novel ATR Inhibitor BAY 1895344 Is Efficacious as Monotherapy and Combined with DNA Damage–Inducing or Repair–Compromising Therapies in Preclinical Cancer Models. *Molecular Cancer Therapeutics* **19**, 26-38 (2020). https://doi.org:10.1158/1535-7163.Mct-19-0019

68 Yap, T. A. *et al.* Camonsertib in DNA damage response-deficient advanced solid tumors: phase 1 trial results. *Nature Medicine* **29**, 1400-1411 (2023). https://doi.org:10.1038/s41591-023-02399-0

69 Dillon, M. T. *et al.* Durable responses to ATR inhibition with ceralasertib in tumors with genomic defects and high inflammation. *The Journal of Clinical Investigation* **134** (2024). https://doi.org:10.1172/JCI175369

70 Gruber, J. J. *et al.* A phase II study of talazoparib monotherapy in patients with wild-type BRCA1 and BRCA2 with a mutation in other homologous recombination genes. *Nature Cancer* **3**, 1181-1191 (2022). https://doi.org:10.1038/s43018-022-00439-1

71 Stolte, B. *et al.* Genome-scale CRISPR-Cas9 screen identifies druggable dependencies in TP53 wild-type Ewing sarcoma. *Journal of Experimental Medicine* **215**, 2137-2155 (2018). https://doi.org:10.1084/jem.20171066

72 Adane, B. *et al.* STAG2 loss rewires oncogenic and developmental programs to promote metastasis in Ewing sarcoma. *Cancer Cell* **39**, 827-844.e810 (2021). https://doi.org:10.1016/j.ccell.2021.05.007

73 Crompton, B. D. *et al.* The genomic landscape of pediatric Ewing sarcoma. *Cancer Discov* **4**, 1326-1341 (2014). https://doi.org:10.1158/2159-8290.Cd-13-1037

74 Wang, W. Y. *et al.* Interaction of FUS and HDAC1 regulates DNA damage response and repair in neurons. *Nat Neurosci* **16**, 1383-1391 (2013). https://doi.org:10.1038/nn.3514

75 Pusch, F. F. *et al.* Elimusertib has Antitumor Activity in Preclinical Patient-Derived Pediatric Solid Tumor Models. *Molecular Cancer Therapeutics* **23**, 507-519 (2024). https://doi.org:10.1158/1535-7163.Mct-23-0094

76 Jess, J. *et al.* Cell Context Is the Third Axis of Synergy for the Combination of ATR Inhibition and Cisplatin in Ewing Sarcoma. *Clin Cancer Res* **30**, 3533-3548 (2024). https://doi.org:10.1158/1078-0432.Ccr-23-3063

77 Henssen, A. G. *et al.* Therapeutic targeting of PGBD5-induced DNA repair dependency in pediatric solid tumors. *Sci Transl Med* **9** (2017). https://doi.org:10.1126/scitranslmed.aam9078

78 Tsherniak, A. *et al.* Defining a Cancer Dependency Map. *Cell* **170**, 564-576.e516 (2017). https://doi.org:10.1016/j.cell.2017.06.010

79 Morgens, D. W., Deans, R. M., Li, A. & Bassik, M. C. Systematic comparison of CRISPR/Cas9 and RNAi screens for essential genes. *Nature Biotechnology* **34**, 634-636 (2016). https://doi.org:10.1038/nbt.3567

80 Evers, B. *et al.* CRISPR knockout screening outperforms shRNA and CRISPRi in identifying essential genes. *Nature Biotechnology* **34**, 631-633 (2016). https://doi.org:10.1038/nbt.3536

81 May, W. A. *et al.* Characterization and Drug Resistance Patterns of Ewing's Sarcoma Family Tumor Cell Lines. *PLOS ONE* **8**, e80060 (2013). https://doi.org:10.1371/journal.pone.0080060

82 Solomon, D. A. *et al.* Mutational inactivation of STAG2 causes aneuploidy in human cancer. *Science* **333**, 1039-1043 (2011). https://doi.org:10.1126/science.1203619

83 Kovar, H. *et al.* Among genes involved in the RB dependent cell cycle regulatory cascade, the p16 tumor suppressor gene is frequently lost in the Ewing family of tumors. *Oncogene* **15**, 2225-2232 (1997). https://doi.org:10.1038/sj.onc.1201397

84 Li, H. & Durbin, R. Fast and accurate long-read alignment with Burrows-Wheeler transform. *Bioinformatics* **26**, 589-595 (2010). https://doi.org:10.1093/bioinformatics/btp698

85 Breese, M. R. & Liu, Y. NGSUtils: a software suite for analyzing and manipulating next-generation sequencing datasets. *Bioinformatics* **29**, 494-496 (2013). https://doi.org:10.1093/bioinformatics/bts731

86 McKenna, A. *et al.* The Genome Analysis Toolkit: a MapReduce framework for analyzing next-generation DNA sequencing data. *Genome Res* **20**, 1297-1303 (2010). https://doi.org:10.1101/gr.107524.110

87 Benjamin, D. *et al.* Calling Somatic SNVs and Indels with Mutect2. *bioRxiv*, 861054 (2019). https://doi.org:10.1101/861054

88 Rausch, T. *et al.* DELLY: structural variant discovery by integrated paired-end and split-read analysis. *Bioinformatics* **28**, i333-i339 (2012). https://doi.org:10.1093/bioinformatics/bts378

89 Tate, J. G. *et al.* COSMIC: the Catalogue Of Somatic Mutations In Cancer. *Nucleic Acids Res* **47**, D941-d947 (2019). https://doi.org:10.1093/nar/gky1015

90 Alexandrov, L. B. *et al.* Signatures of mutational processes in human cancer. *Nature* **500**, 415-421 (2013). https://doi.org:10.1038/nature12477

91 Rosenthal, R., McGranahan, N., Herrero, J., Taylor, B. S. & Swanton, C. DeconstructSigs: delineating mutational processes in single tumors distinguishes DNA repair deficiencies and patterns of carcinoma evolution. *Genome Biol* **17**, 31 (2016). https://doi.org:10.1186/s13059-016-0893-4